Design of electrocatalysts with reduced Pt content supported on mesoporous $NiWO_4$ and $NiWO_4$-graphene nanoplatelets-composite for oxygen reduction and hydrogen oxidation in acidic medium

Int. J. Hydrogen Energy, https://doi.org/10.1016/j.ijhydene.2022.04.270

Simona Somacescu, Petre Osiceanu, Jose Maria Calderon Moreno, Daniela C. Culita, Florentina Neațu, Mihaela M. Trandafir, Ștefan Neațu, Andrei Kuncser, Gábor P. Szijjártó, Emília Tálas, András Tompos, Irina Borbáth*, Mihaela Florea*

Corresponding authors: Irina Borbáth and Mihaela Florea

Received: 6 December 2021/ Received in revised form: 12 April 2022 / Accepted: 12 April 2022

Electronic supplementary material:
The online version of this article (doi: 10.1016/j.ijhydene.2022.04.270) contains supplementary material, which is available to authorized users.

Design of electrocatalysts with reduced Pt content supported on mesoporous $NiWO_4$ and $NiWO_4$-graphene nanoplatelets-composite for oxygen reduction and hydrogen oxidation in acidic medium

Simona Somacescu[a], Petre Osiceanu[a], Jose Maria Calderon Moreno[a], Daniela C. Culita[a], Florentina Neațu[b], Mihaela M. Trandafir[b], Ștefan Neațu[b], Andrei Kuncser[b], Gábor P. Szijjártó[c], Emília Tálas[c], András Tompos[c], Irina Borbáth[c]*, Mihaela Florea[b]*

[a] *"Ilie Murgulescu" Institute of Physical Chemistry, Romanian Academy, Spl. Independentei 202, 060021 Bucharest, Romania*

[b] *National Institute of Materials Physics, 405A Atomistilor Street, 077125 Magurele, Romania*

[c] *Research Centre for Natural Sciences, Institute of Materials and Environmental Chemistry, Eötvös Loránd Research Network (ELKH), Magyar Tudósok Körútja 2, H-1117 Budapest, Hungary*

*Corresponding authors: mihaela.florea@infim.ro (Dr. Mihaela Florea)
borbath.irina@ttk.hu (Dr. Irina Borbáth)

ABSTRACT

Herein, a new direct synthesis route leading to a mesoporous $NiWO_4$ with crystalline framework and $NiWO_4$ - graphene nanoplatelets (GNP) composite is reported. Ni and W assembled into a mesoporous tungstate type of symmetry by co-precipitation synthesis route and its composite with GNP were used as supports for electrocatalysts, with reduced Pt content (8 wt.%), in oxygen reduction reaction (ORR) and hydrogen oxidation reaction (HOR) in acidic medium. A comprehensive assessment of the modifications related to the crystalline and porous structures, morphological aspects as well as the surface chemistry aiming to explain the electrochemical properties was performed. It was found that the presence of GNP during the synthesis process leads, mainly, to the enhanced growth of $NiWO_4$ nanocrystallites, as well as induces changes in the surface chemistry. The electrochemical results show that the introduction of GNPs into the $NiWO_4$ composite support leads to a significant improvement in the activity of the Pt electrocatalyst in ORR and HOR compared to both initial $NiWO_4$ and $Pt/NiWO_4$ samples, as well as mechanical mixtures of these catalysts with carbon. Mass activity for hydrogen oxidation, determined in a mixed kinetic-diffusion controlled region, obtained on the 8 wt. % $Pt/NiWO_4$-GNP catalyst was significantly higher compared to the commercial 20 wt.% Pt/C Quintech catalyst. Our comprehensive structural and surface chemistry assessments indicate this composite material as a viable electrocatalyst for PEMFCs using a broader type of fuels.

Keywords: $NiWO_4$, composite supported electrocatalysts, oxygen reduction reaction, hydrogen oxidation reaction, bifunctional electrocatalysts

1. Introduction

Nowadays, covering the energy demand of humanity without generating toxic or harmful substances is a particularly important challenge. The scientific strategy focuses on the need for cost-competitive low carbon energy and energy efficient technologies. Due to their low operation temperature/pressure requirement and high energy density, Polymer Electrolyte Membrane Fuel Cells (PEMFCs) comprise the most important type of fuel cell for different applications, like automobiles [1–3], stationary [4], and small-scale portable electricity generation [5–7].

Their widespread implementation requires essentially low-cost units with high energy density and durability. Electrocatalysts, which are indispensable elements of the PEMFC electrodes have a vital influence on the performance, durability, and price of the fuel cell [8]. Although significant efforts are spent worldwide on developing novel electrocatalysts for PEM fuel cells, state-of-the-art systems still use catalysts from the Pt/C family [9].

In the last decade a range of oxide-containing electrocatalyst materials [10,11] were proposed for both the hydrogen oxidation reaction (HOR) and the oxygen reduction reaction (ORR). Even if in electrochemical experiments many of oxide-containing electrocatalysts showed excellent properties, its utilization in PEMFCs remains extremely rare. It was proved that the electrochemical properties are strongly affected by the composition of the binary metal oxides used as supports for PtNi nanoparticles deposition [12]. Moreover, the development of efficient, stable and low-cost bifunctional electrocatalysts that could simultaneously catalyse ORR and HOR is highly desirable, and it still represents a big challenge. In general, oxide-containing electrocatalyst materials bring advantages such as reactive hydroxyl groups, which are more easily formed on the oxophilic dopant material than on platinum, and increases the HOR rate [13,14]. Similarly, the better catalytic efficiency of oxide-based Pt electrocatalysts for oxygen reduction is due to the synergistic effect that occurs at the metal oxide–Pt interface, which facilitates the removal of oxygen-containing intermediate particles from the Pt surface, thereby increasing the ORR rate [15–17]. In addition, the agglomeration of metal nanoparticles, known to interfere with the electrocatalyst performances, can be controlled by selecting a proper mixed oxide support that induces specific interactions with the metal. Moreover, the use of oxide increases the resistance to corrosion [10] as well as improves the electrochemical performance related to the ORR with high durability [18].

The interest for binary oxides with multiple valence states like nickel-tungsten mixed oxides ($NiWO_4$) is related to the advantages they offer, such as: inexpensiveness, non-toxicity and electrical conductivity, depending on the calcination temperature [19]. We chose $NiWO_4$ in this work because it is stable in acidic media and it show good proton conductivity. The $NiWO_4$ and its composites have already been found as promising catalysts for a wide scale of chemical reactions such as hydrodesulfurisation [20,21], propane oxydehydrogenation [22], quinoline hydrodenitrogenation [23], catalytic tar removal from biomass gasification [24], reduction of NO [25], cycloaddition of nitrides [26], photocatalytic water splitting [27], etc. The $NiWO_4$ have been described as effective photocatalysts for decomposition of several model pollutants [28–31], too. In addition, $NiWO_4$ nanoparticles and their composites have shown interesting electrochemical properties in various fields including supercapacitors [32–34], electrocatalytic water splitting (both the individual hydrogen evolution (HER) [35] and oxygen evolution (OER), [36,37] half-reactions), electrocatalytic conversion of N_2 to NH_3 [38], etc. Furthermore, the Pt/$NiWO_4$ system has been patented as anode electrocatalysts for alcohol oxidation in fuel cells [39]. It has been supposed that the $NiWO_4$ support removes the carbon monoxide intermediates by creating OH species at the outer surface in aqueous solutions [39]. Moreover, considerable improvement of the ORR activity in an alkaline medium was achieved after loading of 10 wt. % of Pt on a $NiWO_x$ solid solution with plenty of oxygen defects prepared by the displacement of Ni in the $W_{18}O_{49}$ lattice [40].

However, $NiWO_4$ has relatively low electrical conductivity and low specific surface area, which is

disadvantageous when it is applied in electrocatalysts of PEMFC.–These disadvantages can be overcome by combining $NiWO_4$ with a suitable carbonaceous material.

According to literature data, the new types of carbonaceous materials like carbon nanotubes, Ketjen Black carbon and rGOs, etc., provide extreme good properties to metal oxide-carbonaceous composites due to their special electronic structure and also a good conductive host for Pt nanoparticles anchoring [41,42]. Reduced graphene oxide (rGO) was successfully combined with $NiWO_4$ and used in a single-chambered microbial fuel cell [43]; rGO/$NiWO_4$ composites prepared by a hydrothermal method using GO and molten salts $NiWO_4$ exhibited an improved electrochemical performance in the HER in alkaline medium [44], etc. The enhanced electrochemical HER performance and increased long term stability of above rGO/$NiWO_4$ nanocomposite comparing to pure $NiWO_4$ electrodes was attributed to the integration of conducting rGO sheets, which prevent the detachment and agglomeration of nanoparticles. The direct synthesis of the composite was a key issue [44].

Among the new types of carbonaceous materials, pure graphene has excellent electric properties, [45] but it is not yet mass-produced. Contrary, graphene nanoplatelets (GNPs), which are hybrids between the graphene and the graphite, are already industrially available [46]. GNPs exhibit exciting properties such as electrical and thermal conductivity, mechanical toughness, and planar structure with certain amount of oxygen containing functional groups. They can be easily and successfully incorporated into the polymeric matrix [47] and they can slow down the combustion of epoxy composites [48]. Moreover, GNPs are cheaper than carbon nanofibers and nanotubes [46]. Nowadays, there is a growing interest in utilizing GNPs in supercapacitors [49,50], in lithium-ion batteries [51] and in PEM fuel cells [52,53].

It is known that the appropriate porosity of the solid for mass transfer of liquid fuels or oxygen gas and for the minimization of water flooding in electrodes is a key requirement of prospective PEM electrocatalysts [10]. However, just a limited number of works reported about mesoporous $NiWO_4$ developed for electrochemical applications. For example, mesoporous $NiWO_4$ exhibited good performance for photoelectrochemical water oxidation, [54]; mesoporous $NiWO_4$–$CoWO_4$ and carbon-supported Ni–$NiWO_4$@NiS showed a good performance as hybrid supercapacitors [32,55]; mesoporous $NiWO_4$ nanofiber worked as anode for lithium-ion batteries [56].

Thus, we aimed to prepared mesoporous $NiWO_4$ through a facile co-precipitation synthesis route, by using poly(ethylene glycol) (PEG) as template and to use it, as supports for the preparation of catalysts with a relative low (8 wt. %) Pt content. In order to increase both the conductivity and the surface area of our catalysts, the mesoporous $NiWO_4$ was combined with carbonaceous materials, *i.e.* GNP and Black Pearls 2000 carbon. Taking into account that the use of the catalysts with very high Pt content (≥40 wt. %) holds back the large-scale commercialization of PEMFC, the development of the bifunctional active catalyst with lower precious-metal content for both ORR and HOR is highly desirable. We chose to use this material as a bifunctional catalyst mainly due to the low costs generated by our preparation method, its versatility as well as the tailored composition. Therefore, Pt/$NiWO_4$ and Pt/$NiWO_4$–GNP mesoarchitectures were designed for both ORR and HOR in acidic medium for potential use in the PEMFCs. We focused on the synthesis of material containing tungstate structure through a facile synthesis protocol and the corresponding carbonaceous composite, by introducing the GNP in the direct synthesis process. We emphasize the very high yield of our preparation route concomitantly with the structural stability of the catalysts. In addition, the presence of the various Ni and W chemical states, showing a strong interaction with GNP, as well as the low content of Pt is a good prerequisite for using our material as an electrocatalyst in PEM fuel cells.

2. Experimental

2.1. Materials

Ammonium paratungstate ($(NH_4)_{10}W_{12}O_{41}•H_2O$) 99.9%), polyethylene glycol 6000 (PEG), tetrabutylammonium hydroxide solution ((TBAOH) 40 wt. % in H_2O), hydrazine monohydrate (64-65%, reagent grade 98%), polyvinylpyrrolidone ((PVP) average molar weight of 360,000), GNP (with a surface area of 300 m^2/g) and hexachloroplatinic acid hexahydrate ($(H_2PtCl_6•6H_2O)$ 37.5 % Pt) were purchased from Sigma-Aldrich. Sulfuric acid (96% p.a) purchased from Merck was used in this study. Sodium hydroxide NaOH (>98 %), nickel (II) nitrate hexahydrate ($(Ni(NO_3)_2•6H_2O$. p.a., ≥98.5%) were Reanal products. Ethanol (99.55 %), 2-propanol ($(i\text{-}C_3H_5OH)$ 99.9%), ethylene-glycol ((EG) 99.8%) were purchased from Molar Chemicals.

2.2. Synthesis of $NiWO_4$ based electrocatalysts

Mesoporous **$NiWO_4$** powder was prepared by co-precipitation synthesis route by using $Ni(NO_3)_2•6H_2O$ and $(NH_4)_{10}W_{12}O_{41}•H_2O$ as inorganic precursors, PEG as template and TBAOH as pH mediator. The preparation method involved the following steps: 6.0 g $Ni(NO_3)_2•6H_2O$ and 5.2 g $(NH_4)_{10}W_{12}O_{41}•H_2O$ were dissolved in 100 mL deionized water (solution 1). PEG (3 g) was dispersed in 100 mL deionized water (solution 2). The solution 1 was added to solution 2 followed by addition of TBAOH solution under strong stirring conditions to get pH ~13. The resulted mixture was maintained under strong stirring for 24 h and treated for ~ 6 days at 50 °C. The obtained precipitate was dried at 80 °C and calcined in air (2 h at 350 °C for removal of the organic compounds and 8 h at 500 °C to stabilize the tungstate structure, respectively). The heating rate was 2 °C/min.

$NiWO_4$-GNP composite (10 wt.% Graphene nanoplatelets - GNP) was synthesized by the above-described protocol, this time the GNP being added after the pH was adjusted to 13 by using the TBAOH solution. The obtained mixture with a pH~13 was treated for ~ 6 days at 50 °C. The precipitate was dried at 80 °C and calcined in air at 500 °C for 8 h. The heating rate was 2 °C/min.

In order to obtain platinum containing electrocatalyst, the $NiWO_4$ and $NiWO_4$-GNP powders were loaded with 8 wt.% Pt using a modified assisted EG reduction method. Thus, H_2PtCl_6 (167 mg), used as Pt inorganic precursor, was dispersed in ethanol (50 mL), followed by the addition of a solution obtained by mixing 0.3 g PVP with 50 mL ethanol. PVP was used as dispersant for the Pt particles in order to minimize the cluster formation. 0.5 g of support material was suspended in the resulted mixture. After strong stirring for 1 h at room temperature (RT), 20 mL EG was added dropwise and the temperature was increased at 65 °C maintaining the stirring for 4 h. After cooling down at RT, 6 mL hydrazine hydrate solution was added as reducing agent. The suspension was vigorously stirred (1,000 rot/min) for 20 h. The material was separated by centrifugation (15,000 rot/min), washed with water, dried at 80 °C overnight and thermally treated in air at 250 °C to ensure a strong interaction of the Pt particles with the support. These samples are denominated further as **$Pt/NiWO_4$** and **$Pt/NiWO_4$-GNP**.

2.3 Physicochemical characterization

X-ray diffraction analysis were performed on a Bruker D8 apparatus using the following parameters: Cu Kα radiation (λ = 1.5418 Å, 40 kV, 40 mA) at a scanning speed of 0.10 °/min in the 2θ range of 10–90° with a step size of 0.02° and scan time of 1°/min. The average crystallite sizes of prepared composites were measured using Debye-Scherrer's equation.

Raman spectra were obtained on a LabRAM HR Evolution spectrometer from Horiba Jobin Ivon, with a laser radiation at wavelength of 633 nm. All spectra were recorded at room temperature in the extended scan mode in the 50 - 2000 cm^{-1} range.

The N_2 adsorption/desorption isotherms at -196 °C were recorded on a Micromeritics ASAP 2020

analyser. Before analysis the samples were thoroughly degassed under vacuum. Specific surface areas (S_{BET}) were calculated according to the Brunauer-Emmett-Teller (BET) equation, using adsorption data in the relative pressure range between 0.05 and 0.30. The average pore diameter and pore size distribution curves were obtained using Barrett–Joyner–Halenda (BJH) method from the desorption branch.

Scanning electron microscopy (SEM) – The morphological aspects were studied by using a Quanta 3D SEM equipment, operating at 10 kV. In order to correlate topographical features in the micrographs and local variations in composition, secondary (SE) and backscattered (BSE) electrons images were recorded simultaneously on the selected areas.

Transmission Electron Microscopy (TEM) – For microstructural investigations and elemental mappings, a JEOL 2100 TEM (Transmission Electron Microscope) has been used. The instrument was equipped with high resolution polar piece and a JEOL detector for EDS (Energy Dispersive X-Ray Spectroscopy) analysis.

Surface investigation performed by X-ray photoelectron spectroscopy (XPS) was carried out on PHI Quantera equipment with a base pressure in the analysis chamber of 10^{-9} Torr and the monochromatized Al Kα radiation (1486.6 eV). The charging effect was removed by using a dual beam (electrons and Ar ions) as neutralizer while for the binding energy (BE) calibration we used C1s line (BE = 284.8 eV) of the adsorbed hydrocarbon on the sample surface (C–C or $(CH)_n$ bondings).

2.4. Electrochemical characterization

Catalytic activity of the $NiWO_4$-based materials was investigated by rotating disc electrode (RDE) technique in a conventional three-electrode electrochemical glass cell using a Biologic SP150 potentiostate and the EC-LAB software package. The applied electrolyte was 0.5 M H_2SO_4 solution, which was prepared by using Milli-Q water and concentrated H_2SO_4. Electrochemical measurements were carried out at RT. The counter electrode was a platinum wire, while the reference electrode was a hydrogen electrode immersed in the same electrolyte as the working electrode. Potentials are given on the RHE scale.

The working electrode was prepared by dripping a drop of catalyst ink on a freshly polished glassy carbon (GC) electrode (d= 0.3 cm, geometric surface area A= 0.0707 cm^2). For the catalyst ink, 5 mg of powdered catalyst sample was suspended in 4 mL H_2O + 1 mL isopropanol + 20 µL Nafion solution (D520 Nafion Dispersion - Alcohol based 1000 EW at 5 wt.%, DuPont™ Nafion®). The suspension was sonicated for 30 minutes. From this suspension a drop (3.6 µL) was pipetted on to the dry mirror-polished GC and dried at room temperature for 30 min.

Sufficient electronic conductivity of the GNP-free $NiWO_4$ and $Pt/NiWO_4$ samples was ensured by preparation of mechanical mixture of starting catalysts with 20 wt. % BP carbon (BP: Black Pearls 2000 (CABOT)). For this purpose, these materials were mixed in a mortar with carbon with a wt.%/wt.% ratio of 80/20 and then rotated with a tube rotator (VWR) for 24 hours. Mechanical mixture of BP carbon with $NiWO_4$ and $Pt/NiWO_4$ was denominated as $NiWO_4$-BP and $Pt/NiWO_4$-BP, respectively.

Before the measurements the electrolyte was purged with Ar for at least 20 minutes then 10 cyclic voltammograms (CVs) were recorded with 100 mV s^{-1} sweep rate between 50 and 1000 mV for conditioning the catalysts as described before in ref [57]. After the activation procedure, CV measurements were done in the potential range of 50-1000 mV at a scan rate of 10 mV s^{-1}.

The ORR measurements were done in O_2 saturated 0.5 M H_2SO_4 solution at ambient temperature and pressure. Polarization curves were recorded by sweeping the potential between 300 and 1000 mV with 10 mVs^{-1} sweep rate, rotating the electrode at 225, 400, 625, 900, 1225 and 1600 revolutions/min (rpm). Data were obtained from the negative scans.

Catalytic activity in the HOR was also investigated by RDE method in hydrogen saturated 0.5 M

H_2SO_4 solution at 400, 625, 900, 1225 and 1600 rpm rotating speed of the electrode. Polarization curves were recorded by sweeping the potential between 0 and 300 mV with 10 mVs^{-1} sweep rate.

For comparison activity in the ORR and HOR commercially available reference 20 wt.% Pt/C (Quintech, C-20-Pt, on Vulcan; denoted hereafter as 20Pt/C) electrocatalyst was also studied by the same methods as described above.

3. Results and discussion

3.1. Structural analysis

3.1.1. X-Ray diffraction. The XRD pattern of nickel tungsten oxide powder, the sample $NiWO_4$ (Fig. 1a), corresponds to one phase with monoclinic symmetry, space group P2/c, lattice parameters values a = 4.60, b = 5.66, c = 4.91 Å, (quasi-orthorhombic, β = 90.01°) in good agreement with JCPDS cards 72-1189 and 72-0480 for $NiWO_4$ (2θ = 19.28°, 23.97°, 24.91°, 30.96°, 36.62°, 41.72° and 54.68° were ascribed to the (100), (011), (110), (111), (002), (121) and (202) hkl planes of monoclinic phase structure of $NiWO_4$ [58]. The XRD pattern of $Pt/NiWO_4$ sample corresponds to a $NiWO_4$ major phase of identical symmetry with $NiWO_4$ powder, and additional peaks that can be indexed to cubic Pt phase. The crystallite sizes were calculated from half peak widths using Scherrer's equation, giving values of 22 nm for $NiWO_4$ and 19/25 nm for $Pt/NiWO_4$ nanocrystallites.

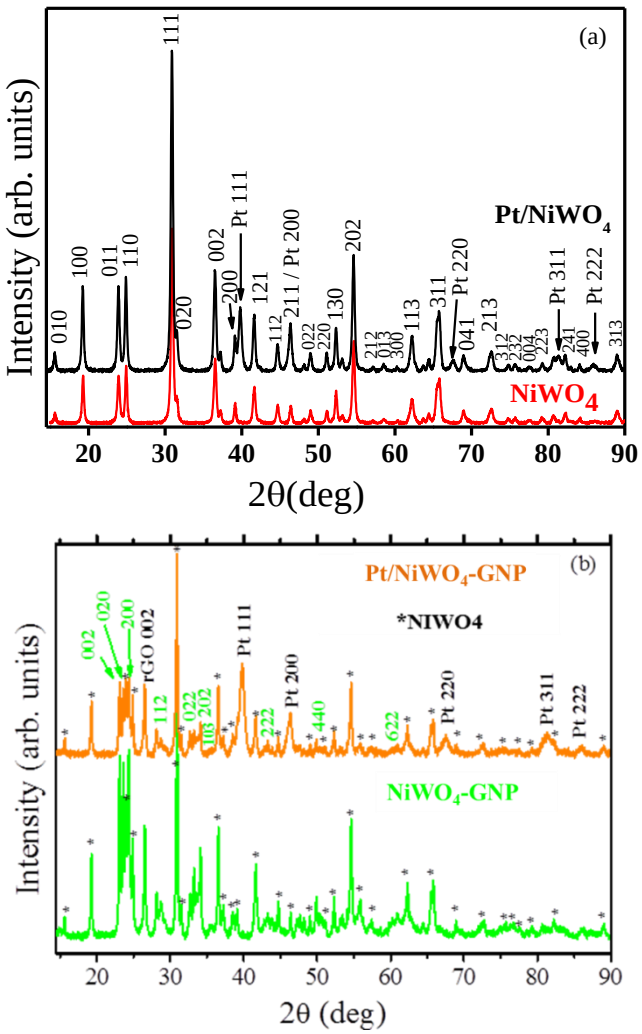

Figure 1. XRD patterns for $NiWO_4$, $Pt/NiWO_4$, $NiWO_4$-GNP and $Pt/NiWO_4$-GNP

The XRD pattern of sample $NiWO_4$-GNP (Fig. 1b) corresponds to a mixture of two tungsten containing phases, one with the same symmetry as monoclinic $NiWO_4$, and the second one tungsten oxide WO_3, also with monoclinic symmetry, space group P21/c. Additionally, the 002 peak of graphitic carbon from GNP can be detected at ~27°. The XRD pattern of Pt/$NiWO_4$-GNP corresponds to the same phases, but with lower content of the oxide WO_3, and additional peaks that are indexed to cubic Pt phase. The presence of weak cubic NiO peaks cannot be excluded, but peak overlapping with other phases precludes a precise quantification. According to the literature, the relative low calcination temperature can result in NiO and WO_3 traces [59]. The crystallite sizes were calculated from half peak widths using Scherrer's method, giving values of 42/33 nm for $NiWO_4/WO_3$ and 14/36/28 nm for Pt/$NiWO_4/WO_3$ nanocrystallites.

3.1.2. Raman Spectroscopy. The Raman spectra of $NiWO_4$ and Pt/$NiWO_4$, recorded under ambient conditions, are presented in Fig. 2a. As can be observed, in both cases, the presence of the characteristic WO_3 vibrations at around 803, 712 and 268 cm^{-1} show the impurification of the tungstate materials, even though, X-ray diffraction on $NiWO_4$ did not evidence this phase, but it is well known that Raman spectroscopy is a more sensitive technique for structural modifications compared with X-ray diffraction. For the other samples containing GNP, Raman results are in good agreement with the XRD data.

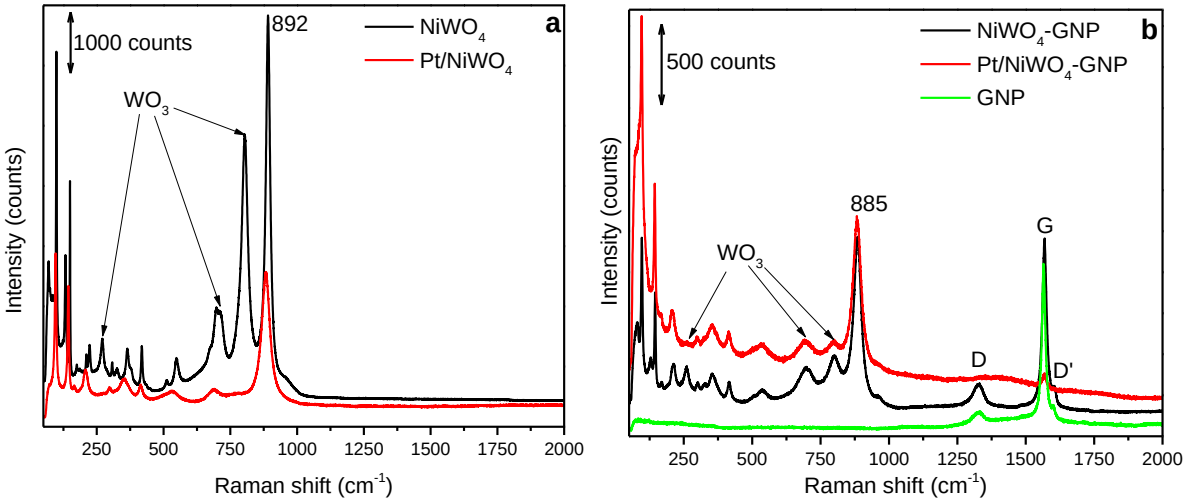

Figure 2. Raman spectra of $NiWO_4$-based materials and related Pt-containing catalysts prepared without (a) and with GNP addition (b)

$NiWO_4$ possesses, besides the WO_3 bands, Raman features at 892, 699, 548, 511, 418, 364, 307, 223, 149, and 98 cm^{-1}, with the most intense band located at 892 cm^{-1} being assigned to the WO_6 symmetric stretching vibration [60,61]. The observed vibrational modes below 600 cm^{-1} are related to a lattice phonon, which involves the motion of distorted octahedral [NiO_6] clusters, while the vibrational modes above 600 cm^{-1} are related to the vibration of the distorted octahedral [WO_6] clusters in the lattice [62,63]. Pt/$NiWO_4$ sample presents the same Raman features as the $NiWO_4$ material. Thus, the Pt/$NiWO_4$ Raman spectrum from Fig. 2a shows the presence of already specified specific bands assigned to both [WO_6] and [NiO_6] clusters. However, it should be noted that Pt deposition is accompanied by a decrease in the intensity of all these Raman features.

The presence of GNP phase in the composites is demonstrated clearly by the corresponding D and G bands of graphene [64] (see Fig. 2.b). The spectrum recorded for pure GNPs (see Fig. 2.b) shows the characteristic D, G of graphene at 1329 and 1572 cm^{-1} [64]. The D band corresponds to the breakdown of translational symmetry generated by the microcrystalline structure, while the G band is

assigned to the Raman-active E_{2g} mode for the tangential in-plane stretching vibrations of the sp^2-hybridized bond [65]. The I_D/I_G ratio is a measure of the degree of defects present in the sample and the in-plane crystalline size of the sample. Thus, the calculated I_D/I_G ratios of $NiWO_4$-GNP (0.50) and Pt/$NiWO_4$-GNP (0.84) are higher than that of the GNP (0.46), suggesting that the former samples possess more defects than GNP after $NiWO_4$ and Pt introduction. The in-plane crystallite size (L_a) of the samples calculated from the Tuinstra-Koenig relation (L_a (nm) = $(2.4 \times 10^{-10}) \lambda^4 (I_D/I_G)^{-1}$),[66] where λ is the Raman excitation wavelength (633 nm in our case) were found to be 77 nm, 46 nm and 84 nm for the $NiWO_4$-GNP, Pt/$NiWO_4$-GNP and GNP, respectively. As during the sample preparation $NiWO_4$-GNP was subjected to calcination in air at 500 °C to get crystalline $NiWO_4$, a larger extent of oxidation of the carbonaceous part, consequently much larger I_D/I_G ratio compared to the pure GNP would have been expected. However, oxidation of GNP in composites differs significantly from that of traditional carbonaceous supports, *i.e*. activated carbons; GNPs are believed to seal oxide grain boundaries and hinder the further influx of oxygen [67] and drastically slows down heat conduction and migration of decomposed volatiles to the surface by creating improved char structures [68]. In contrast, the introduction of metallic Pt onto the $NiWO_4$-GNP composite changed the I_D/I_G ratio much more dramatically; it can be imagined that Pt settled on not only the $NiWO_4$ but on the carbonaceous part, disturbing its symmetry. Another, less likely option is that local hydrogenation of the aromatic system occurs when the metal Pt is formed during hydrazine reduction.

3.2. Textural assessment

The textural properties of the $NiWO_4$–based samples were assessed by N_2 adsorption-desorption analysis. Table 1, Fig. 3 and Fig. S1 summarize the data obtained from the adsorption-desorption isotherms.

Table 1. Textural properties of the $NiWO_4$–based samples

Sample	SSA (m^2/g)	Average pore size (nm)
$NiWO_4$	25.4	17.0
Pt/$NiWO_4$	22.4	23.4
$NiWO_4$-GNP	28.8	2 - 4 / ~35
Pt/$NiWO_4$-GNP	27.7	4 / ~35

The N_2 adsorption-desorption isotherms for $NiWO_4$ and Pt/$NiWO_4$ display classical type IV curve accompanied by H3 type hysteresis loops, according to IUPAC classification [69], typical for mesoporous materials with large pores (Figs. 3a-d). The capillary condensation phenomenon in mesopores occurs at high relative pressures ($p/p_0 > 0.8$) and adsorption saturation is not visible. The specific surface areas (SSAs) were found to be 25.4 m^2/g for $NiWO_4$ and 22.4 m^2/g for Pt/$NiWO_4$ (see Table 1). It is interesting to note that SSA of $NiWO_4$ used for catalytic hydrodesulfuration [22] was in the same range (30 m^2/g). It has also been reported that specific surface area of pure $NiWO_4$ decreased with the increasing temperature of calcination linearly [59]. The introduction of 10 wt.% GNP into the composite only slightly increased its SSA, in line with the literature results [70].

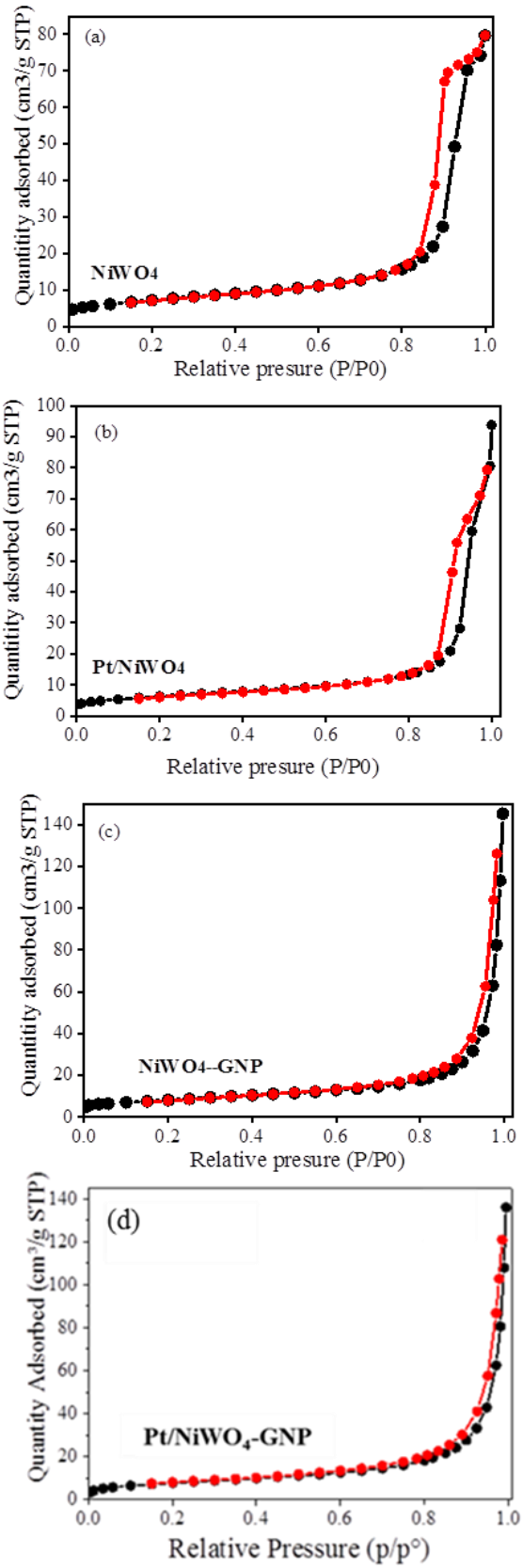

Figure 3. Nitrogen adsorption-desorption isotherms

The BJH pore size distribution curves show monomodal distribution for both samples (Figs. S1a,

b) with an average pore size of 17.0 nm for $NiWO_4$ and 23.4 nm for $Pt/NiWO_4$. In the case of $NiWO_4$-GNP the isotherm has the same profile as the other two samples, but the hysteresis loop appears at higher relative pressure which indicates the presence of larger pores. A close examination of the BJH distribution graph reveals a wide pore size distribution with a small fraction ranging from 2 to 4 nm (Figs. S1c, d), while most of them cover the domain characteristic of mesopores, and even more. The analysis performed on pure GNP thermally treated at the same temperature as the composite (not shown) indicate that the small pores fraction is attributable to GNP.

3.3. Morphological investigation

3.3.1. Scanning Electron Microscopy (SEM). SEM micrographs at different magnifications of $NiWO_4$ and $Pt/NiWO_4$ nanoparticles are gathered in Fig. 4; $NiWO_4$ nanocrystallite sizes are ~ 20-30 nm, in agreement with X-ray diffraction data. Figs. 4a-d are taken in SE image mode, displaying topological contrast. BSE images (Figs. 4e-f) were recorded simultaneously from the same areas for $Pt/NiWO_4$. In spite of the lower resolution and higher noise to signal ratio intrinsic to the BSE images compared to SE images, because BSE images are obtained from a much lower number of electrons (those back-scattered), the Z (atomic mass)-contrast allows the identification of Pt presence: the bright shapes in BSE images (Figs. 4e-f) are Pt and the grey ones $NiWO_4$ nanoparticles. Pt nanocrystallite sizes are ~ 40-50 nm.

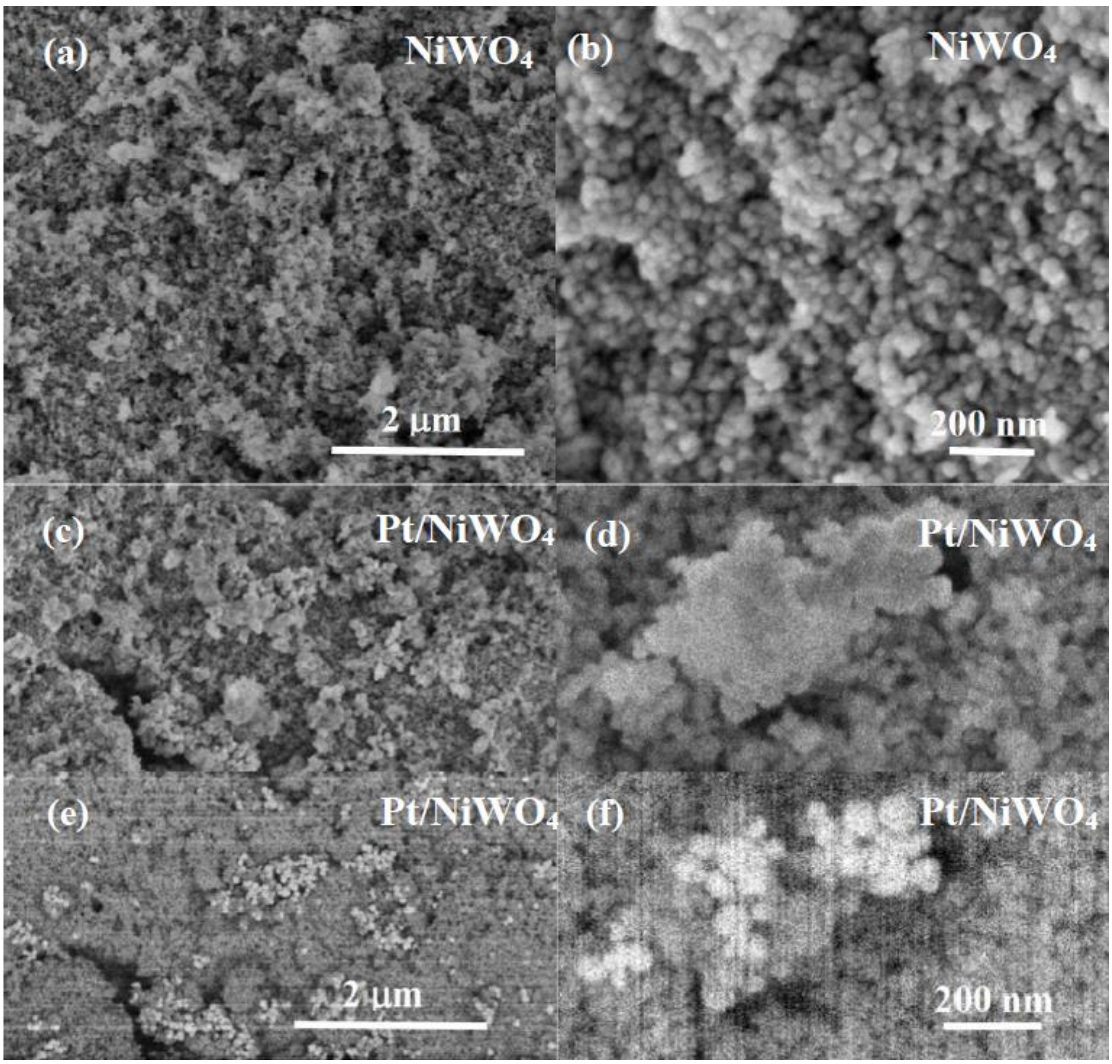

Figure 4. SEM micrographs at different magnifications of (a-b) $NiWO_4$ and (c-d) $Pt/NiWO_4$ nanoparticles; (e-f) BSE images of the same areas shown in c and d

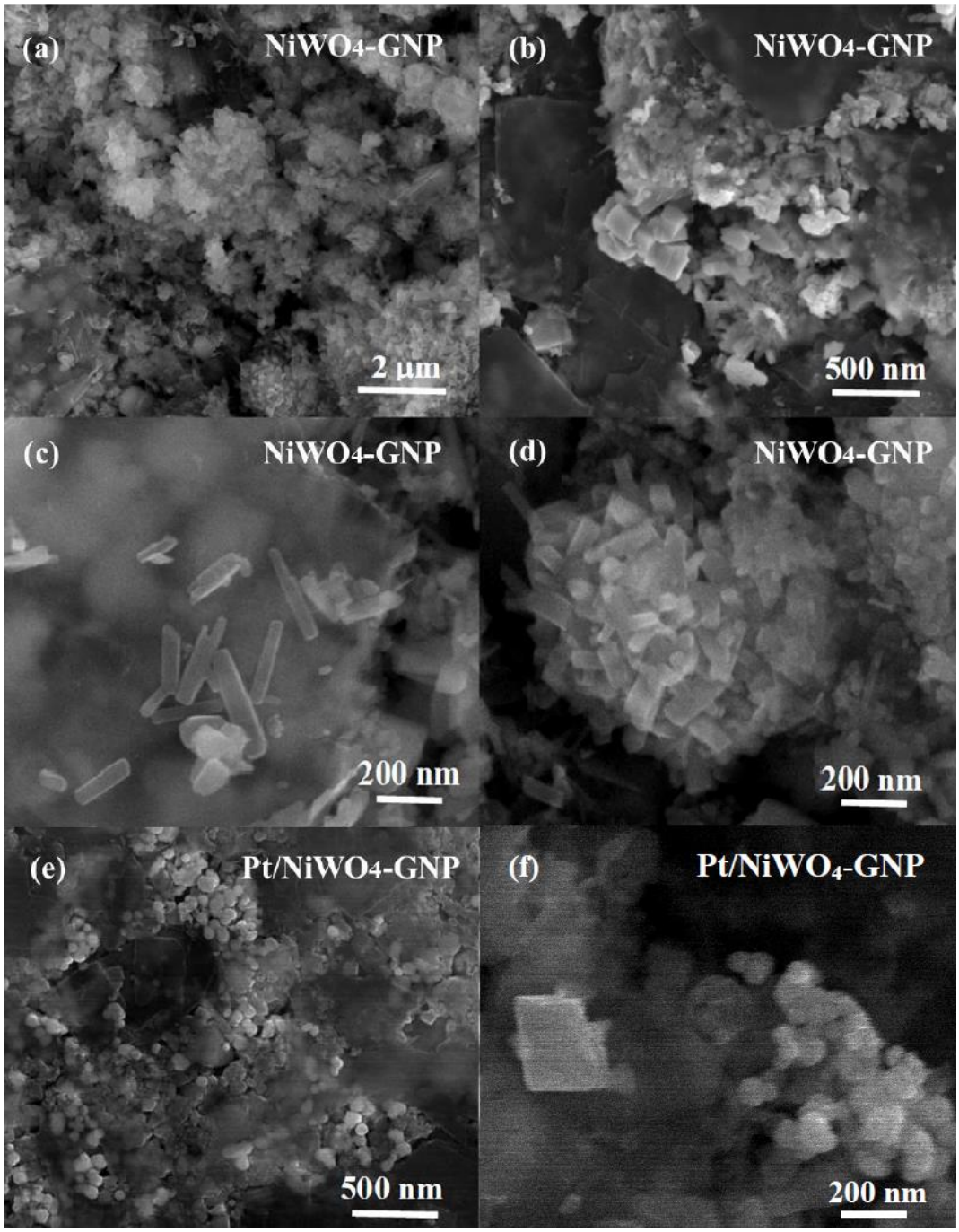

Figure 5. SEM micrographs at different magnifications of (a-d) $NiWO_4$-GNP: general view of the sample, details showing faceted $NiWO_4$ crystallites and GNP flakes (darker), and (e-f) Pt/$NiWO_4$-GNP, showing faceted $NiWO_4$, GNP flakes and rounded Pt nanoparticles

SEM micrographs at different magnifications of $NiWO_4$-GNP are presented in the Figs. 5 a-c: Fig. 5a shows a general view of the sample; Fig. 5b shows at higher detail faceted $NiWO_4$ crystallites and GNP flakes (darker), and Fig. 5c illustrates the dispersion of $NiWO_4$ elongated platelets lying on GNP flakes, compared to Fig. 5d of one aggregate of $NiWO_4$ crystallites, at the same magnification. The SEM study indicates that the presence of GNP promotes the growth of $NiWO_4$ crystallites, significantly bigger and clearly faceted, compared to the equiaxed nanocrystallites observed in $NiWO_4$ and Pt/$NiWO_4$.

SEM micrographs of Pt/$NiWO_4$-GNP at different magnifications are depicted in Figs. 5e-f, where

we can observe clusters of Pt nanoparticles as rounded, bright particles, at the edges of GNP flakes (Fig. 5e) and faceted $NiWO_4$ crystallites; the image at higher magnification (Fig. 5f) shows on faceted $NiWO_4$ crystallite on GNP, near a cluster of rounded Pt nanoparticles.

3.3.2. Transmission Electron Microscopy (TEM).

The morphology has also been investigated by conventional Transmission Electron Microscopy (TEM), the structure has been identified by Selected Area Electron Diffraction (SAED) and the compositional homogeneity has been checked by Scanning Transmission Electron Microscopy (STEM) coupled with Energy Dispersive X-Ray Spectroscopy (EDS). Results are shown in Figs. 6-9.

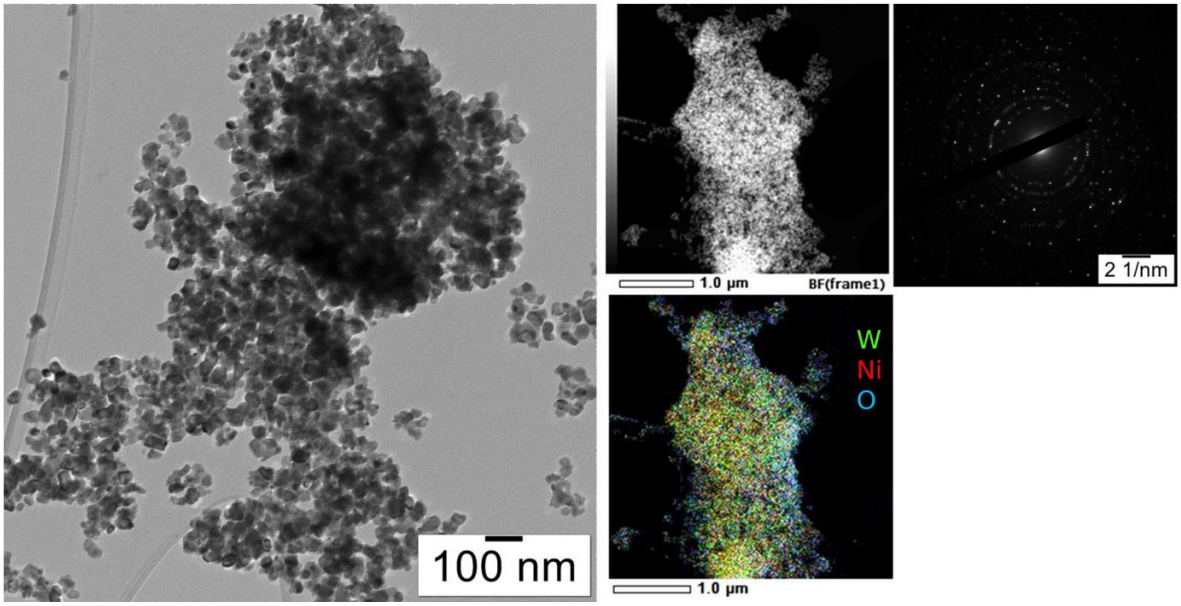

Figure 6. CTEM (left column), STEM-EDS (middle column) and SAED (right column) on $NiWO_4$

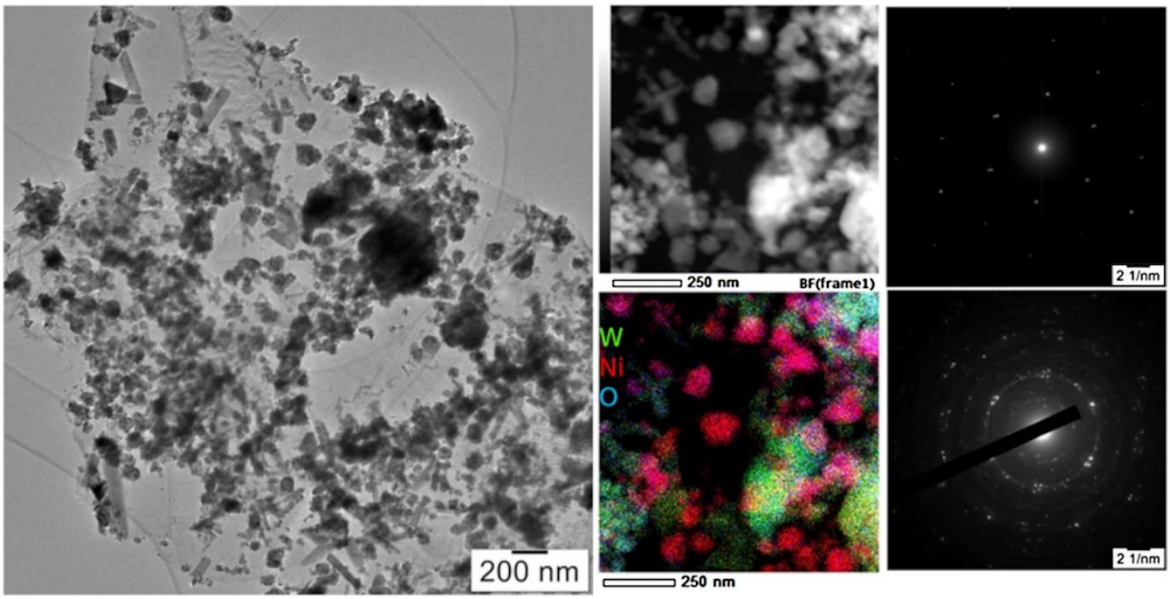

Figure 7. CTEM (left column), STEM-EDS (middle column) and SAED (right column) on $NiWO_4$-GNP

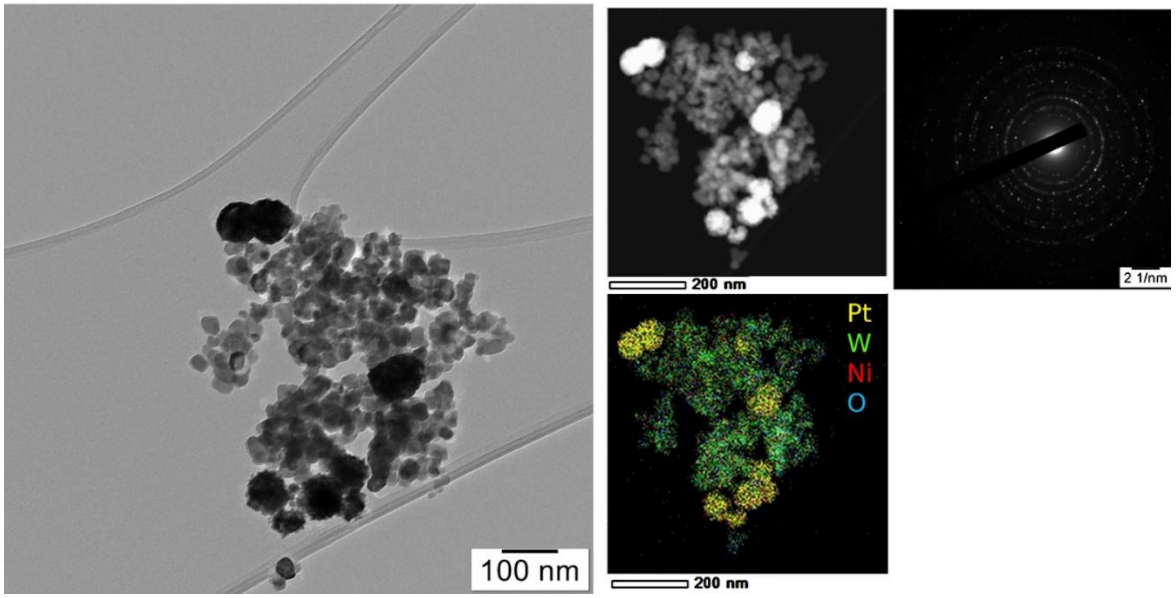

Figure 8. CTEM (left column), STEM-EDS (middle column) and SAED (right column) on $Pt/NiWO_4$

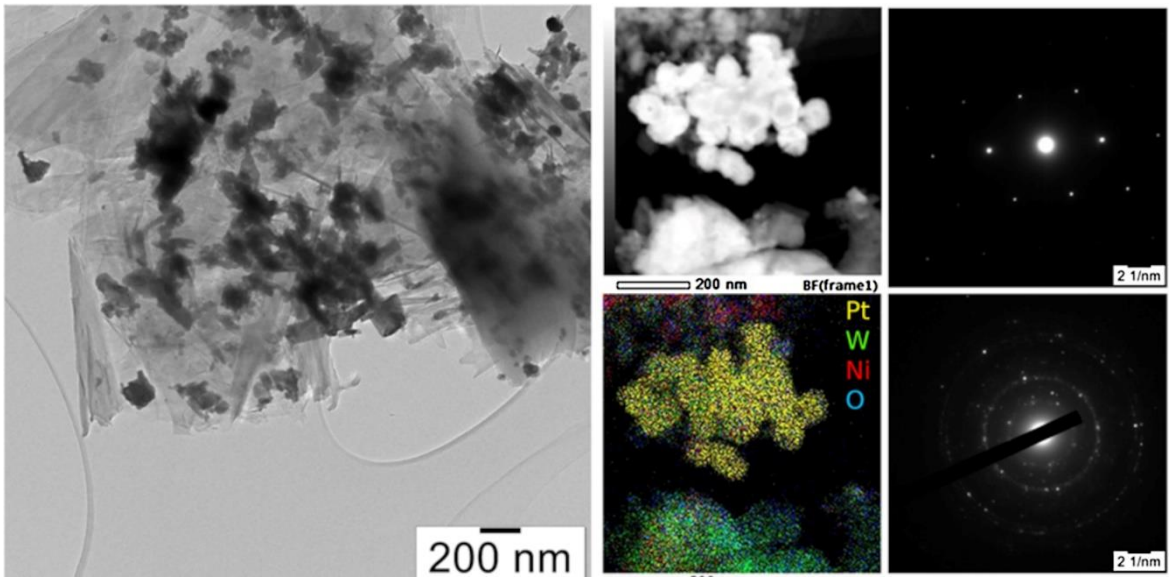

Figure 9. CTEM (left column), STEM-EDS (middle column) and SAED (right column) on $Pt/NiWO_4$-GNP

The $NiWO_4$ sample shows ~27 nm crystalline nanoparticles with relatively homogenous size and shape distribution, in agreement with SEM and X-ray diffraction data (Fig. 6). The $NiWO_4$ structure (space group 13) has been identified by SAED whereas the EDS maps show a good compositional homogeneity. The $NiWO_4$-GNP sample (Fig. 7) shows graphene sheet containing crystalline entities with a wide shape and size distribution. The system shows compositional inhomogeneity, with Ni based compounds segregated in big clusters (~100 nm). SAED investigations revealed the presence of GNP sheet, while the presence of the $NiWO_4$, evidenced by X-ray diffraction, remains yet uncertain. The $Pt/NiWO_4$ system is composed of ~30 nm well crystallized $NiWO_4$ nanoparticles (space group 13) with relatively homogenous size and shape distribution and a sub-system of spherical Pt clusters with ~50 nm diameter (Fig. 8). Excepting the presence of Pt, the $Pt/NiWO_4$ sample is similar to the parent $NiWO_4$. The $Pt/NiWO_4$-GNP sample morphology (Fig. 9) is similar to the parent $NiWO_4$-GNP excepting the presence of Pt clusters of ~100 nm which is similar to the one observed in $Pt/NiWO_4$.

The GNP sheet was identified by SAED, whereas the $NiWO_4$, as in the case of the parent $NiWO_4$-GNP, structure remains yet uncertain.

3.3.3. Surface chemistry characterization by X-ray Photoelectron Spectroscopy (XPS). After collecting survey (wide scan) spectra (not shown here) for a review of the elements present on the surface layer (< 10 nm), the high-resolution spectra were recorded for the most prominent photoelectron lines: C1s, O1s, $Ni2p_{3/2}$, W4f and Pt4f (Figs. 10 and 11). We estimate that our experimental errors for the Binding Energies (BEs) assignments are within ± 0.2 eV while for the quantitative analysis (relative concentrations) in the range of ± 5%. For the BEs and intensity accurate calibration as well as for data processing and interpretation we followed the ISO-TC201 ("Surface Chemical Analysis" – SCA) recommendations. Figs. 10a-d show the superimposed, normalized $Ni2p_{3/2}$ and W 4f high resolution spectra (Figs. 10a and 10b) as well as the $Ni2p_{3/2}$ and W4f deconvoluted XPS spectra for the samples containing GNPs (Figs. 10c and 10d). A careful examination of the superimposed spectra clearly reveals some differences that occur for the samples without/with GNPs incorporated that were highlighted by the deconvolution procedure.

Thus, for the samples without GNP, Ni is present on the surface only as Ni^{2+} coordinated in the monoclinic tungstate lattice ascribed to the (BE) ~855.9 eV (Fig. 10a). Nevertheless, the tails towards lower BEs in the spectra with graphene nanoplateles (GNPs) suggest the presence of an additional Ni^{2+} species, probably due to the interaction with the GNPs. In addition, the formation of the tinny amount of NiO on the top of the surface cannot be ruled out in agreement with the XRD results for the bulk analysis. The peak found at ~858 eV is assigned to the multiplet (MS) and energy loses (EL) splittings[71,72], while the broad peak ~862 eV is attributed to the characteristic satellite [73] associated to $Ni2p_{3/2}$.

A more pronounced asymmetry can be observed in the superimposed and normalized W 4f spectra (Fig. 10b) mainly for $NiWO_4$-GNP sample clearly suggesting the formation of the different W chemical species. A close inspection of these spectra points out a more pronounced splitting of the W4f doublet for the samples without graphene ($NiWO_4$ and $Pt/NiWO_4$), while the GNP containing composite and the related Pt catalyst ($NiWO_4$-GNP and $Pt/NiWO_4$-GNP) show quite different split and shape, mainly for the $NiWO_4$-GNP sample, which is a feature of the existence of additional oxidation states accommodated under the spectra envelope.

Therefore, we proceeded with the spectral fitting for the latter one (Fig. 10d) showing that the W remains mainly bonded in the tungstate structure assigned for the BE of $W4f_{7/2}$~ 35.4 eV. In addition, the fitting process distinctly proves the presence of the 6+ oxidation characteristic to the WO_3 ($W4f_{7/2}$, BE = 36.4 eV), in good agreement with XRD results. Moreover, as a result of the method sensitivity, XPS is able to detect W, on the outermost surface layer with lower valence state 5+ assigned for the BE ~ 34.5 eV. The quantitative assessment led to the following results: W mainly bonded in the tungstate structure (60.5%), W^{6+} in the WO_3 symmetry (12.8%) and W^{5+} (26.7%). The presence of these different W chemical species, working in concert, creates defects on the surface as oxygen vacancies. This peculiar behaviour could be explained by the effect of GNP [67], introduced by direct synthesis which promotes a different growth of $NiWO_4$ faceted crystallites with formation of W secondary phases. The graphene is incorporated in the lattice and a strong interaction with Ni occurred. Consequently, an amount of W was separated as secondary phase in the full oxidation state (WO_3) as well as a mixture (e.g., W^{5+}/W^{6+}) of valence states. One can notice that the Pt deposition procedure leads to a significant decrease of W^{6+} from WO_3 and W^{5+} percentages (Fig. 10b). Overall, we find out that the surface chemistry investigations point out a good agreement and complementarity with the XRD and Raman results supporting the data consistency.

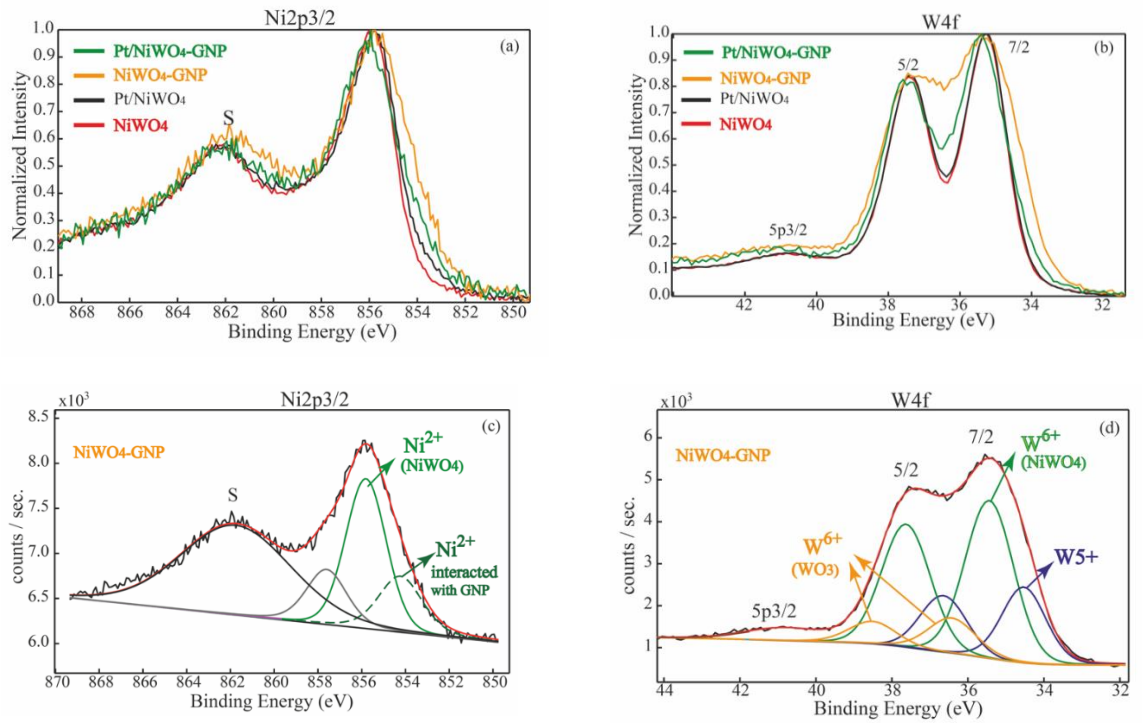

Figure 10. The high resolution, superimposed Ni $2p_{3/2}$ and W 4f spectra for the $NiWO_4$-based catalysts (a, b) and the deconvoluted $Ni2p_{3/2}$ (c) and W4f (d) photoelectron spectra for the $NiWO_4$-GNP sample.

Figs. 11a and 11b exhibit the superimposed, normalized Pt4f photoelectron spectra for $Pt/NiWO_4$ and $Pt/NiWO_4$-GNP samples, displaying a quite similar behaviour. The Pt content, for the both samples, detected on the surface by XPS was ~ 9.1 wt. %, slightly higher than the nominal percentage probably due to a segregation tendency from the bulk to the surface. Following the fitting procedure, we find out that Pt is present on the surface mainly (~83%) as metallic Pt (BE~ 71 eV ±0.2 eV) together with a contribution of ~ 17% as $Pt(OH)_2$ formed, most probably, from the OH adsorbed groups on the top of the surface.

The oxygen chemistry was assessed from the analysis of the O1s singlet (Figs. 11c and 11d). Thus, the superimposed and normalized O1s spectra (Fig. 11c) display an asymmetry towards higher BEs more pronounced for the samples with incorporated GNPs, as a result of the additional C–O functionalities groups associated to the graphene. O1s spectral deconvolution (Fig. 11d) shows three components assigned, as follows: ~530.4 eV – oxygen bonded in the oxide lattice, ~531.7 eV OH adsorbed groups and C–O functionalities from graphene and ~533 eV a small amount of adsorbed water.

GNP incorporated into the wolframite structure was extensively detected on the surface by XPS. Thus, in order to assess the carbon chemistry, we made the spectral deconvolution (Fig. 11e), as follows: the sp^2 (67.4%) and sp^3 (15.7%) hybridized carbons were assigned to the BEs of 284.5 ± 0.2 eV and 285.3 ± 0.2 eV, respectively. One can observe the contribution of the oxygen functional groups (16.9%), accommodated on the higher BEs side of the spectra: (C–O: 286.3 eV (~11.0%), C=O: 287.8 eV (~5.0%), C–O=O: 288.9 eV (~0.9%)) in line with the standard GNPs in the as received stage. One can notice that C1s spectrum recorded on the GNP-free sample ($Pt/NiWO_4$) (Fig. S2) revealed the presence only of the adventitious carbon located at 284.8 eV used for BEs calibration.

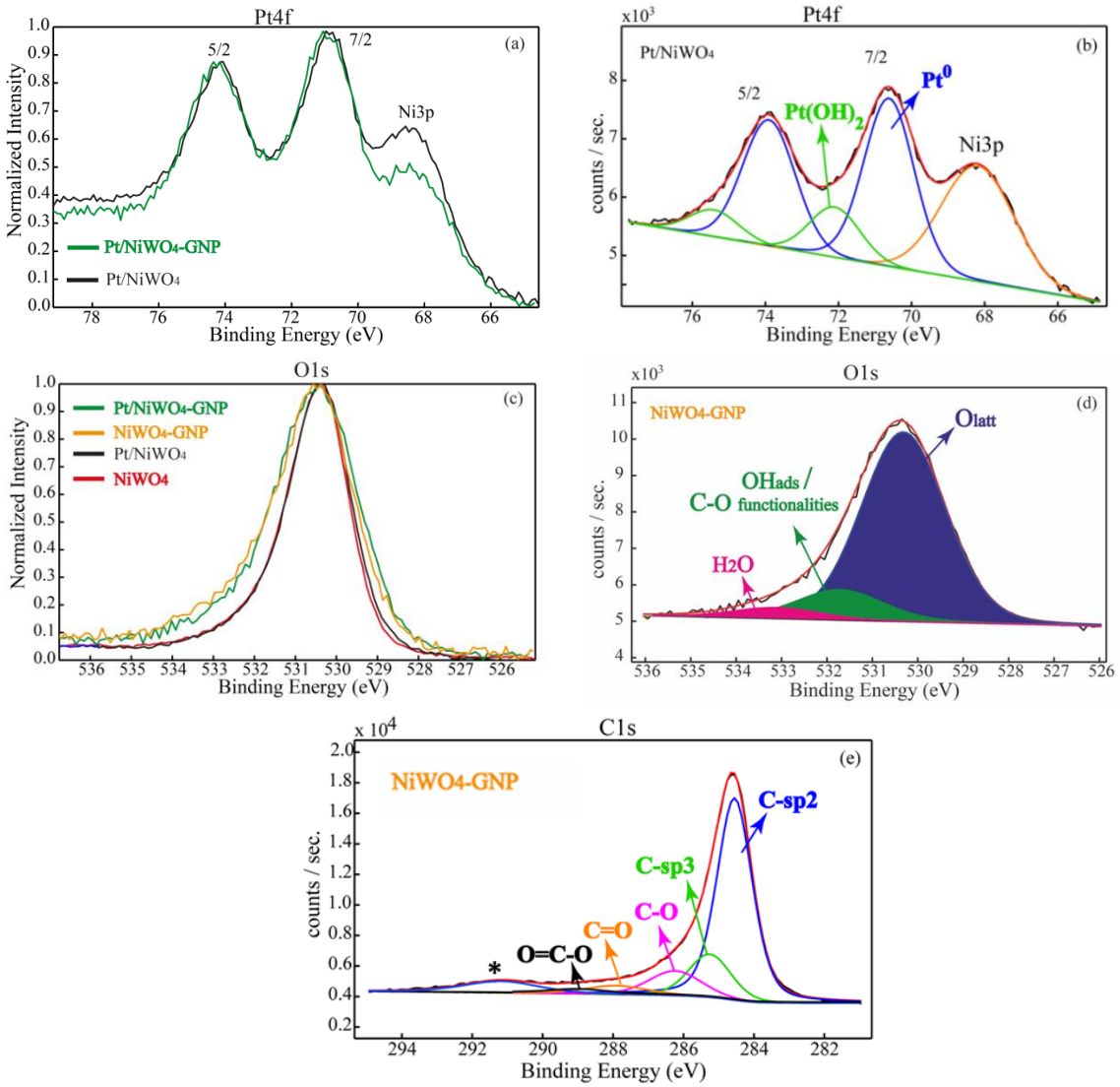

Figure 11. The high resolution, superimposed Pt 4f and O1s spectra (a, c) and the deconvoluted photoelectron Pt4f (b), O1s (d), C1s (e) spectra for the $NiWO_4$-based samples.

3.4. Electrochemical characterization

In order to clarify the possibility of using these novel materials as cathode and/or anode in PEM fuel cells, their electrochemical characteristics were investigated. The corresponding cyclic voltammograms are presented in Fig. 12a and Fig. S3 (top) of the Supplementary Materials. Since the $NiWO_x$ solid solution with mixed valence oxides can exhibit electrical conductivity or semiconductivity, initially the samples were tested without mixing with carbon. However, as shown in Fig. 12a, the CVs of the carbon-free $NiWO_4$ and $Pt/NiWO_4$ electrodes indicated no peaks in the studied range. The addition of carbon resulted in slightly distorted rectangular curves with significantly wider hysteresis, indicating an increase in capacity compared to samples without carbon as a result of better electrolyte access to the electrode surface. The presence of 8 wt. % of Pt in the samples reflected in some increase of the peak associated with adsorption of under potentially deposited hydrogen (H_{upd}) on Pt surface. A comparison of the electrocatalytic behavior of the initial $NiWO_4$ and 8 wt. % $Pt/NiWO_4$ samples with the results obtained on mechanical mixtures of these catalysts with carbon was also demonstrated in Figs. S3a and S3b, respectively.

The electrocatalytic performance of the $NiWO_4$-based catalyst materials in the ORR (Fig. 12b and Fig. S3 (middle)) and the HOR (Fig. 12c and Fig. S3 (bottom)) was evaluated by polarization curves

measurements. It should be noted that after carbon addition, sizable increase of the ORR activity was observed only on the Pt/$NiWO_4$ catalyst (Fig. 12b and Fig. S3 (middle)), but the activity of the Pt/$NiWO_4$-BP in the HOR remains negligible (Fig. 12c and Fig. S3 (bottom)). In this series of experiments, the best activity in the ORR and the HOR was obtained on the Pt catalyst supported on $NiWO_4$-GNP composite (Fig. S3c).

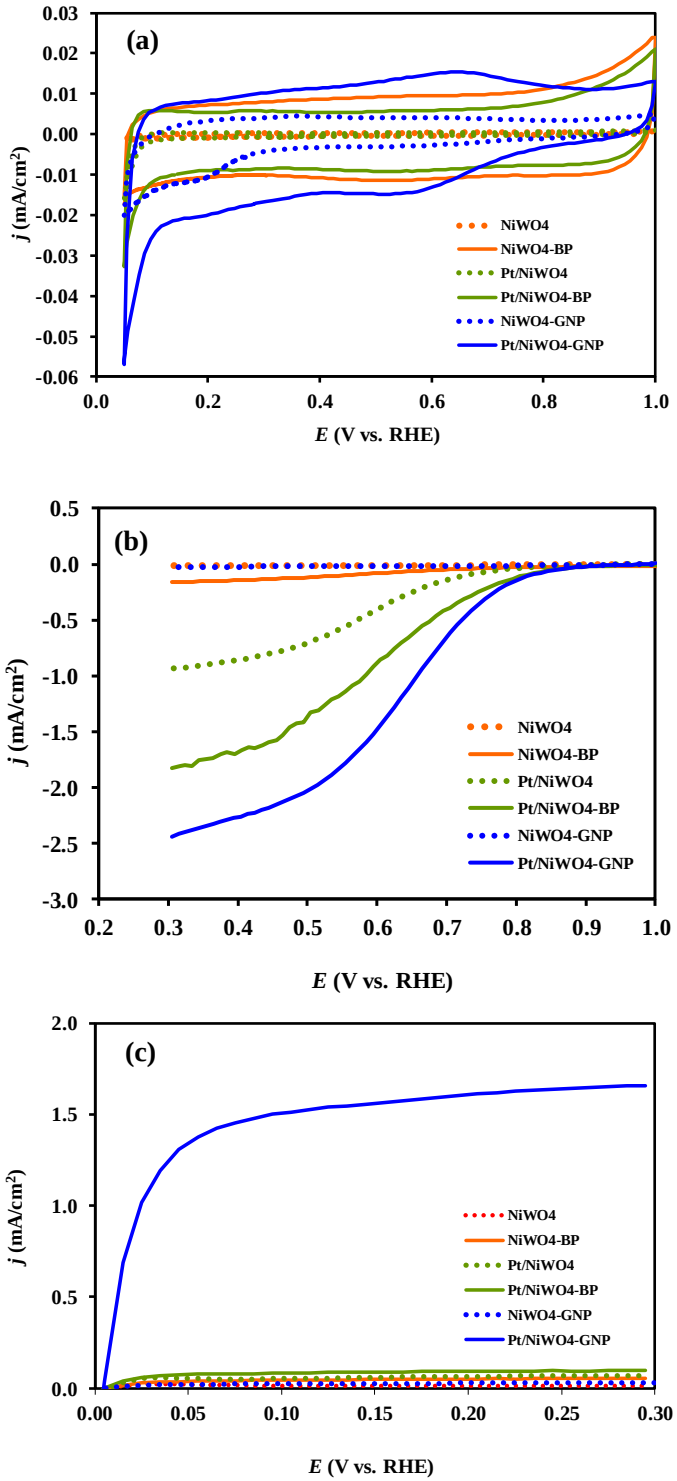

Figure 12. Electrochemical characterization of the $NiWO_4$-based electrocatalysts: (a) Cyclic voltammograms obtained with and without addition of 20 wt.% BP carbon; (b) ORR curves obtained in O_2-saturated 0.5 M H_2SO_4 on a rotating disc electrode (RDE) at 1600 revolutions/min (rpm); (c)

HOR curves obtained in a H_2-saturated 0.5 M H_2SO_4 on a RDE at 1600 rpm. Sweep rate: 10 mV s^{-1}, T = 25 °C.

In our recent study [74], it has been demonstrated that a significant increase in ORR activity was observed on the $NiCo_2O_4$–NiO catalysts after mixing with 10 wt. % rGO, which provides more efficient mass transfer, higher stability and better resistance to deactivation during ORR.

As an illustration, the polarization curves of GNP-containing catalyst obtained in the ORR and HOR at different potentials and rotation rates were presented in Figs. S4a and S5a of the Supplementary Materials, respectively. Results obtained on the reference 20Pt/C sample in both reactions were demonstrated in Figs. S4b and S5b.

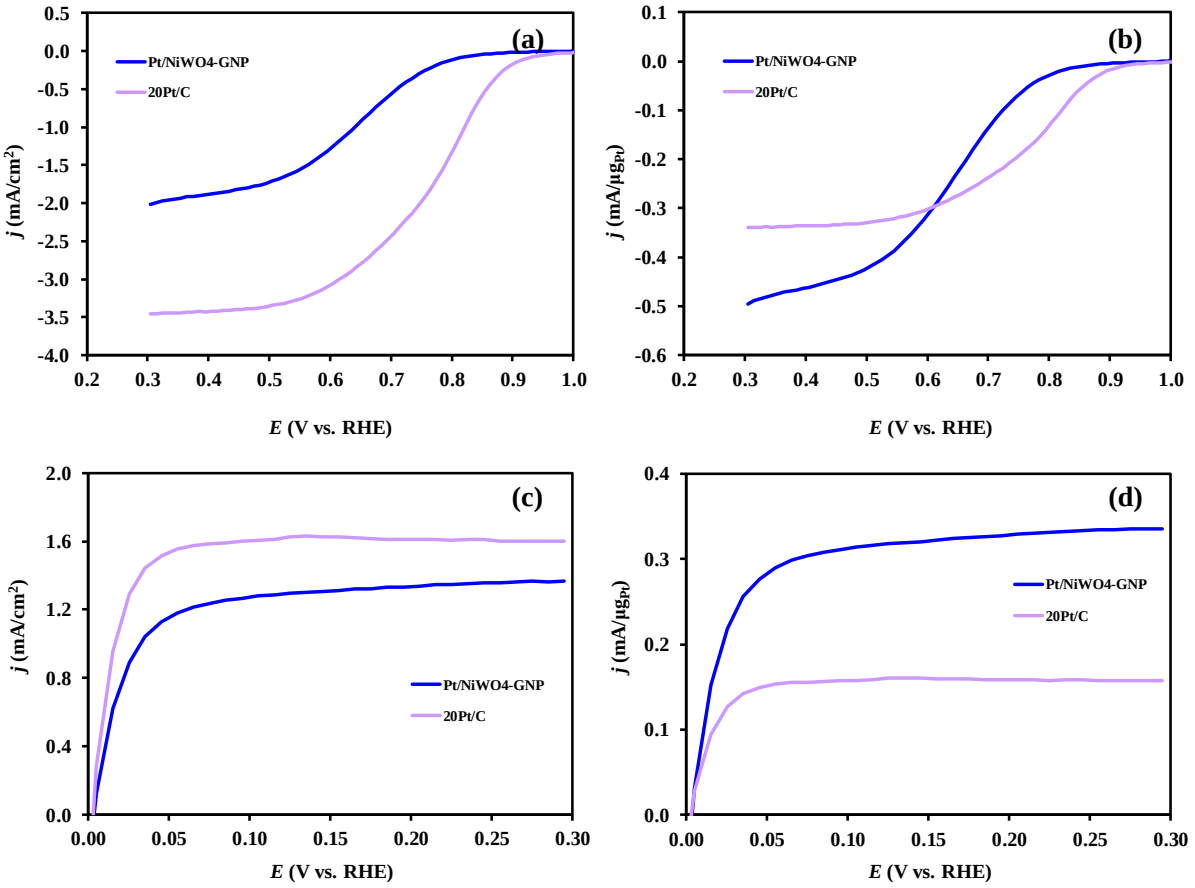

Figure 13. Electrocatalytic performance of the Pt/$NiWO_4$-GNP and reference 20Pt/C electrocatalysts in the ORR (top row) and the HOR (bottom row) measured in 0.5 M H_2SO_4 at 900 rpm: (a, c) in units of mA/cm^2 and (b, d) mass activity in units of mA/μg_{Pt}. *j* vs. *E* curves were obtained at 10 mV s^{-1} sweep rate. The Pt loading of the electrodes was 4.1 μg cm^{-2} and 10.2 μg cm^{-2} for Pt/$NiWO_4$-GNP and 20Pt/C catalysts, respectively.

The activities of our best electrocatalyst, Pt/$NiWO_4$-GNP, and the commercial reference, 20 wt.% Pt/C, in ORR and HOR were compared on Fig. 13 (top row) and 13 (bottom row), respectively. In order to compare the activities of the catalysts current values normalized to the geometric surface area of the electrode were depicted in Fig. 13a and 13c. However, in the case of catalysts with different Pt content the presentation of the results expressed as mass specific current densities is more correct (see Fig. 13b and 13d).

Despite the fact that diffusion limiting current density of the Pt/$NiWO_4$-GNP sample was higher

than that of the 20Pt/C catalyst (Fig. 13b), the onset potential of the ORR was observed at less positive potential, indicating that this catalyst is less active. Moreover, the mixed kinetics-diffusion control region of the reference 20Pt/C is in the range from 0.6 V and 1.0 V, but the diffusion-limited current density plateau was not reached on the catalyst with 8 wt.% content of Pt (see Fig. 13b), demonstrating that this catalyst does not perform well in the ORR.

At low potentials the current densities obviously depend on the rotating rates, indicating that the oxygen reduction is diffusion limited. As shown in Fig. 14a, linear relationship of Koutecky - Levich plot was obtained between the square root of the rotation rate ($\omega^{-1/2}$) and the current density (j^{-1}) corresponding to the diffusion-limited potential region at 300 mV potential for the Pt/$NiWO_4$-GNP and 20Pt/C electrocatalysts.

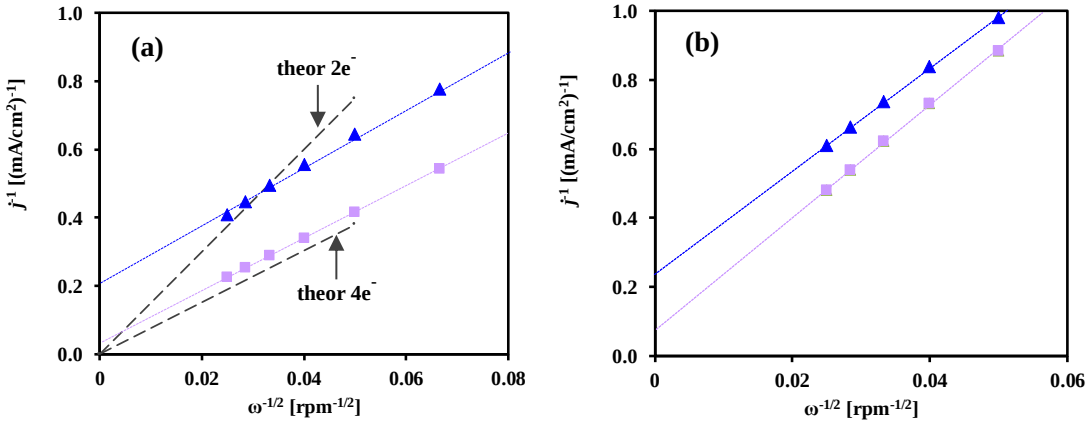

Figure 14. Koutecky - Levich representation of ORR (a) and HOR (b) measurements obtained on the (▲) Pt/$NiWO_4$-GNP and (■) 20Pt/C electrocatalysts.

First, the linearity of the Koutecky - Levich plots confirms the reliability of the RDE measurements. The electron transfer number for the ORR can be estimated from the slope of this plot in spite of the complexity of the electrode processes [75–77]. The theoretical Koutecky - Levich plot for four- and two-electron pathways was also included in Figure 14a. To obtain maximum energy capacity, it is highly desirable to reduce O_2 via the $4e^-$ pathway. As emerges from Fig. 14a on both catalysts the ORR proceed with the same reaction mechanism. As can be seen from Figure 14a the obtained slope for theoretical $4e^-$ route (n= 4) is in good agreement with the value of the slope obtained experimentally for both electrocatalysts. Moreover, according to the Koutechky - Levich representation of the data the electrode reaction in all cases was under mixed kinetic-diffusion control at this potential.

It has been mentioned [78,79] in that interpretation of the results of RDE measurements obtained on electrocatalysts with large surface area and disperse surface should be carried out cautiously. Nevertheless, in the present study catalysts with similar composition and structure were investigated applying the same procedure and electrode preparation technique and the RDE results may contribute to their qualitative description and comparison.

Certainly, it is desirable to have the ORR occurring at potentials as close as possible to the reversible (thermodynamic) electrode potential with a satisfactory reaction rate. The Tafel equation indicates a linear relationship between the logarithm of current and electrode potential (for details see Supplementary Materials). Conventionally, the Tafel analysis leads to two important physical parameters: the Tafel slope and the exchange current density [80,81].

It has been demonstrated that in the ORR reaction on Pt catalysts, the Tafel slope varies greatly depending on the applied potential, since the reaction orders also change at different potentials [82].

The measured Tafel slope, including its shift from about ~60 mV/decade of current at low overpotential to ~120 mV/ decade at higher overpotential, is consistent with the initial electron transfer as the sole rate-limiting step over the entire range of operating potentials [83].

The results of the Tafel analysis performed for the $Pt/NiWO_4$-GNP and 20Pt/C catalysts were presented in Table S1 of the Supplementary Materials. When determining the proper overvoltage range, it was necessary to take into account that the loading of Pt in the electrodes was different: 4.1 μg cm^{-2} and 10.2 μg cm^{-2} for $Pt/NiWO_4$-GNP and 20Pt/C catalysts, respectively. This is important to consider for the following reason: it has been demonstrated [84] that when evaluating the kinetic current at the given potentials (e.g. 0.9 V), appropriate catalyst loading should be carefully considered to ensure the reaction is in the kinetics region with Tafel slope smaller than 120 mV/decade (this is especially important when increased Pt loading was used).

The polarization curves were fitted with two slopes: a low and high Tafel slope obtained at low and high overpotentials, respectively. In our calculations, in accordance with the recommendations given in ref. [85], we used overvoltage values not higher than $\eta \leq -413$ mV, since diffusion effects begin to interfere with the kinetics of the electrode. The similarity between the Tafel slopes shown in Table S1 suggests the same reaction mechanism on these two catalysts. The best fits yielded the Tafel slope of -119 mV/decade for $Pt/NiWO_4$-GNP and -122 mV/decade for 20Pt/C catalyst, supporting one-electron transfer in the rate-determining step with the corresponding transfer coefficients equal to 0.50 and 0.48, respectively. As shown in Table S1, at a Tafel slope of ~-120 mV/decade, for the $Pt/NiWO_4$-GNP and 20Pt/C catalysts the values of the exchange current densities, which depend not only on the Tafel slope, but also on the number of Pt sites involved, were 2.98×10^{-5} and 2.64×10^{-4} mA/cm^2, respectively.

According to the literature the exchange current densities on various electrocatalysts in two regions are around 10^{-7} and 10^{-4} mA/cm^2. For instance, in ref. [86] the exchange current densities for the Pt/C and Pt–Fe/C catalysts with 60 wt.% Pt loading, determined at 60 °C in the region characterized by 120 mV/decade Tafel slope, were 1.63×10^{-5} mA/cm^2 and 2.15×10^{-4} mA/cm^2, respectively.

It was demonstrated in ref. [87] that the addition of tungsten carbide nanocrystals to Pt on carbon led to an increase in the exchange current densities in both high and low overpotential regions by two orders of magnitude, demonstrating a synergistic effect of improving activity for ORR. It should be noted that the exchange current density obtained on the starting 40 wt.% Pt/C catalyst in the region of -62 mV/decade was three orders of magnitude lower compared to the values obtained at ~-122 mV/decade (5.25×10^{-7} and 3.16×10^{-4} mA/cm^2, respectively).

The value calculated for the $NiWO_4$-containing catalyst at -57 mV/decade was even smaller, about 8.01×10^{-8} mA/cm^2. For the 20Pt/C with Pt loading of 10.2 μg cm^{-2} in the low overvoltage region, a similar value was obtained. However, possibly due to the high content of Pt, this region was too short and therefore there may be a lot of uncertainty in the calculation.

Figs. 13c-d display HOR voltammograms (positive-going scans) recorded via the RDE technique in H_2-saturated 0.5 M H_2SO_4 on the $Pt/NiWO_4$-GNP and 20Pt/C electrocatalysts. As can be seen from Fig. 13c the electrochemical performance of the 8 wt. % $Pt/NiWO_4$-GNP catalyst, presented as current values normalized to the geometric surface area of the glassy carbon electrode, was comparable to that obtained on the commercial Pt/C catalyst with 20 wt. % Pt loading.

It should be noted that the HOR proceeds on the platinum group metals at a very high rate. Thus, at the maximum possible electrode rotation speeds and low hydrogen solubility in water and electrolyte, the measured currents, even near the equilibrium potential, are mainly determined by the hydrogen diffusion rate in the solution [88]. On both polarization curves the steady-state current rises sharply from the origin with positive going potential and reaches a limiting plateau above 50 mV. The limiting current density of the $Pt/NiWO_4$-GNP catalyst is only slightly lower than that of the reference

20Pt/C.

The electrocatalytic activity for H_2 oxidation obtained on commercial 20Pt/C and Pt/$NiWO_4$-GNP catalysts at different rotation rates was presented on Fig. S5 in the Supplementary Materials. Koutecky - Levich plot of $1/j$ versus $\omega^{-1/2}$ obtained from the results of the diffusion-limited potential region at 250 mV was shown in Fig. 14b. As can be seen from Fig. 14b, rather similar slope 6.2×10^{-2} and 6.8×10^{-2} (mA/cm^2) rpm$^{-1/2}$ of Koutecky - Levich plot was obtained on the 20Pt/C and Pt/$NiWO_4$-GNP catalysts, respectively.

These values are close to the theoretical value 6.54×10^{-2} (mA/cm^2) rpm$^{-1/2}$ obtained in 0.5 M H_2SO_4 at 25 °C [89] and correspond to the experimental value for a smooth platinum electrode.

The intercept of a dependence extrapolated to an infinite rotation rate with the ordinate corresponds to the reciprocal of the kinetic current density of the HOR at a potential of 250 mV. According to the Koutechky - Levich representation of the data the electrode reaction in both cases is under mixed kinetic-diffusion control at 250 mV. The values for kinetic current densities of the Pt/$NiWO_4$-GNP and 20Pt/C catalysts were 4.1 and 12.8 mA/cm^2, respectively. It should be noted that the catalysts were used without any purification procedure (purification in oxidizing mixture, treatment in hydrogen, etc.) [90], which is generally recommended in the case of kinetic studies and may result in an increase in kinetic currents from 3.8 to 9 mA/cm^2. Moreover, it has been demonstrated [91] that a sufficiently precise evaluation of kinetic component, j_k, from the total current density, j, and the value of diffusional component (j_d) at the corresponding rotation rate can be done if the determined values of j_k are less than ca. 7 mA/cm^2.

As shown in Fig. 13d, mass activity for hydrogen oxidation, determined in the mixed kinetic-diffusion controlled region, obtained on the Pt/$NiWO_4$-GNP catalyst was significantly higher comparing to the commercial 20Pt/C catalyst.

Thus, the use of a new mesoporous $NiWO_4$-GNP composite as a support for Pt electrocatalysts has shown promising HOR activity, due most probably to the presence of both, WO_3 and $NiWO_4$, in this sample as revealed by XRD and XPS analysis. Indeed, it is well-documented that atomic hydrogen can be reversibly stored in tungsten trioxide [92]. Hydrogen tungsten bronzes H_xWO_3 ($0.3<x<0.5$), which is an acid resistant metallic conductor, could function as intermediates in the anodic oxidation of hydrogen, providing an alternative path for the reaction [93]:

$$WO_3 + x\ Pt\text{-}H \rightarrow H_xWO_3 + Pt \rightarrow WO_3 + x\ e^- + x\ H^+ \qquad (1)$$

Moreover, the proton conducting tungsten bronze provides rapid hydrogen oxidation leading to the improvement of the overall catalytic activity [93,94]. The increased activity of WO_3/$NiWO_4$ nanocomposites with respect to methanol oxidation was associated with the involvement of WO_3 in the formation of hydrogen bronzes, followed by the migration of the H atom to $NiWO_4$ oxides leading to the formation of $NiWO_4$-OH_{ads}, which ensured resistance to CO by a bifunctional mechanism [95].

It is well known that metal species with different size (single atoms, nanoclusters, and nanoparticles) show different catalytic behavior [96]. In addition, many factors, including the particle size, shape, chemical composition, metal−support and metal−reactant/solvent interactions, significantly affect the catalytic properties of metal catalysts. It has recently been demonstrated that strong metal-support interaction and the size of Pt clusters has a great influence on the electrochemical performance in ORR and HOR of the 1–7 wt.% Pt/GNS (GNS: graphene nano sheets) catalysts [97].

In order to find the correlation between particle size and activity, our future research on this topic will focus on optimizing the deposition of Pt onto $NiWO_4$-GNP composite materials in order to increase the dispersion of Pt and improve the metal-support interaction.

4. General assessments

In summary, we successfully synthesized mesoporous $NiWO_4$ and its composite with GNP,

through a versatile approach that involves a direct co-precipitation method. The obtained tungstates and their composite, were used as supports for deposition of 8 wt.% Pt. Based on XRD, SEM, XPS and TEM results, the prepared $NiWO_4$ was a single phase of nickel tungstate. Nevertheless, the composite material obtained following the same chemical route, with GNP introduced by direct synthesis, exhibits modifications in the crystalline framework, morphology as well as in the surface chemistry. The presence of the sp^2 and sp^3 hybridized carbon in the composite material, characteristic to GNP, was proved by the spectral fitting of C1s photoelectron line. XRD pattern of the $NiWO_4$-GNP composite revealed a mixture of two tungsten containing phases, one monoclinic $NiWO_4$ and the second one, tungsten oxide WO_3, also with monoclinic symmetry, space group P21/c. The surface chemistry assessed by XPS confirms quantitatively the aforementioned findings with W^{6+} detected mainly bonded in the $NiWO_4$ structure (60.5%), compared with W^{6+} in the WO_3 symmetry (12.8%); in addition, a fraction of W with lower valence state (W^{5+} ~26.7%) was highlighted by XPS, able to generate a defected surface leading to the formation of the oxygen vacancies. By Pt deposition a significant decrease of the WO_3 and W^{5+} percentages occurred, most probably due to the effect of hydrazine used as reducing agent in the deposition step. Platinum was found mainly as metallic Pt with a low percentage of $Pt(OH)_2$, due to the presence of hydroxyl groups on the surface, clearly revealed in the O1s deconvoluted singlet. According to XPS results, Ni^{2+} was detected on the surface mainly coordinated into $NiWO_4$ structure with a small fraction of Ni^{2+} in interaction with the GNPs.

We found that the incorporation of GNP into $NiWO_4$ clearly leads to an improvement in the HOR and ORR performances in comparison with catalytic systems that represent a mechanical mixture of the starting $NiWO_4$ and Pt/$NiWO_4$ electrocatalysts with 20 wt.% BP carbon.

These findings can be associated with a higher concentration of lattice defects and active sites as a result of the presence of the W^{6+}/W^{5+} redox couple, as well as to the strong interaction between GNP -$NiWO_4$ - Pt. Moreover, the bigger nanocrystallites clearly faceted and $NiWO_4$ elongated platelets lying on the GNP flakes as well as the broader pore size distribution with a small fraction ranging from 2 to 4 nm ease the mass transport of the reactant's molecules to the Pt metallic active sites. We have to emphasize that Pt/$NiWO_4$-GNP exhibited an enhanced catalytic activity in HOR.

5. Conclusions

The mesoporous composite $NiWO_4$-GNP bifunctional catalyst showed a better electrochemical performance, as a result of the beneficial role played by GNP introduced by direct synthesis. The synergic phenomena between the $NiWO_4$ and GNP were induced by the direct synthesis route leading to a growth of $NiWO_4$ faceted crystallites with different W valence states (W^{6+}/W^{5+}). Addition of Pt to $NiWO_4$-GNP induces an improvement in HOR, and also generates a final composite that is more efficient than the commercially available 20Pt/C material, if we take into account the Pt loading of the electrodes. This behaviour is a result of the synergy of the bifunctional $NiWO_4$-GNP material and the reduced Pt content. Thus, the presence of defects and of a special morphology of the $NiWO_4$-GNP facilitate the mass transfer of reactants to Pt active sites. Our comprehensive structural and surface chemistry assessments indicate this composite material as a viable catalyst for PEMFCs using a broader type of fuels.

Acknowledgments

This work was performed within the framework of the "Holistic design of fuel cell electrocatalysts for the least power applications" (CATALEAST) M-ERA.NET project. Project No. NNE 131270 has been implemented with the support provided from the National Research, Development and Innovation Fund of Hungary financed under the M-ERA.NET funding scheme. This work was also supported by the Romanian National Authority for Scientific Research and Innovation, CCCDI – UEFISCDI, project numbers 111/2019 and 110/2019, M-ERANET-CATALEAST, within PNCDI III

and Core Program PN19-03 (contract no. 21 N/08.02.2019).

References

[1] Reddy KJ, Sudhakar N. ANFIS-MPPT control algorithm for a PEMFC system used in electric vehicle applications. Int J Hydrogen Energy 2019;44:15355–69. https://doi.org/10.1016/j.ijhydene.2019.04.054.

[2] Ao Y, Laghrouche S, Depernet D, Chen K. Lifetime prediction for proton exchange membrane fuel cell under real driving cycles based on platinum particle dissolve model. Int J Hydrogen Energy 2020;45:32388–401. https://doi.org/10.1016/j.ijhydene.2020.08.188.

[3] Zhang X, Zhou J, Chen W. Data-driven fault diagnosis for PEMFC systems of hybrid tram based on deep learning. Int J Hydrogen Energy 2020;45:13483–95. https://doi.org/10.1016/j.ijhydene.2020.03.035.

[4] Crespi E, Guandalini G, Gößling S, Campanari S. Modelling and optimization of a flexible hydrogen-fueled pressurized PEMFC power plant for grid balancing purposes. Int J Hydrogen Energy 2021;46:13190–205. https://doi.org/10.1016/j.ijhydene.2021.01.085.

[5] Ghodba A, Sharifzadeh M, Rashtchian D. Integrated and inherently safe design and operation of a mobile power generation: Process intensification through microreactor reformer and HT-PEMFC. Int J Hydrogen Energy 2021;46:23839–54. https://doi.org/10.1016/j.ijhydene.2021.04.176.

[6] Gatto I, Saccà A, Pedicini R, Passalacqua E, Carbone A. Evaluation of titanium oxide introduction in the electrode structure for portable PEMFC applications. Int J Hydrogen Energy 2021;46:27687–99. https://doi.org/10.1016/j.ijhydene.2021.05.200.

[7] P. Ferreira-Aparicio and A. M. Chaparro. Portable Hydrogen Energy Systems: Fuel Cells and Storage Fundamentals and Applications. Elsevier; 2018.

[8] Neaţu Ş, Neaţu F, Chirica IM, Borbáth I, Tálas E, Tompos A, et al. Recent progress in electrocatalysts and electrodes for portable fuel cells. J Mater Chem A 2021;9:17065–128. https://doi.org/10.1039/d1ta03644k.

[9] Fan L, Zhao J, Luo X, Tu Z. Comparison of the performance and degradation mechanism of PEMFC with Pt/C and Pt black catalyst. Int J Hydrogen Energy 2022;47:5418–28. https://doi.org/10.1016/j.ijhydene.2021.11.135.

[10] Zhang Z, Liu J, Gu J, Su L, Cheng L. An overview of metal oxide materials as electrocatalysts and supports for polymer electrolyte fuel cells. Energy Environ Sci 2014;7:2535–58. https://doi.org/10.1039/C3EE43886D.

[11] Samad S, Loh KS, Wong WY, Lee TK, Sunarso J, Chong ST, et al. Carbon and non-carbon support materials for platinum-based catalysts in fuel cells. Int J Hydrogen Energy 2018;43:7823–54. https://doi.org/10.1016/j.ijhydene.2018.02.154.

[12] Martins M, Milikić J, Šljukić B, Soylu GSP, Yurtcan AB, Bozkurt G, et al. Mn_2O_3-MO (MO = ZrO_2, V_2O_5, WO_3) supported PtNi nanoparticles: Designing stable and efficient electrocatalysts for oxygen reduction and borohydride oxidation. Microporous Mesoporous Mater 2019;273:286–93. https://doi.org/10.1016/J.MICROMESO.2018.07.022.

[13] Elezović NR, Gajić-Krstajić LM, Vračar LM, Krstajić N V. Effect of chemisorbed CO on MoO_x–Pt/C

electrode on the kinetics of hydrogen oxidation reaction. Int J Hydrogen Energy 2010;35:12878–87. https://doi.org/10.1016/j.ijhydene.2010.09.004.

[14] Santiago E, Batista MS, Assaf E, Ticianelli E. Mechanism of CO Tolerance on Molybdenum-Based Electrocatalysts for PEMFC. J Electrochem Soc 2004;151.

[15] Yan Z, Xie J, Jing J, Zhang M, Wei W, Yin S. MoO_2 nanocrystals down to 5 nm as Pt electrocatalyst promoter for stable oxygen reduction reaction. Int J Hydrogen Energy 2012;37:15948–55. https://doi.org/10.1016/j.ijhydene.2012.08.033.

[16] Martins PFBD, Ticianelli EA. Electrocatalytic Activity and Stability of Platinum Nanoparticles Supported on Carbon–Molybdenum Oxides for the Oxygen Reduction Reaction. ChemElectroChem 2015;2:1298–306. https://doi.org/10.1002/celc.201500196.

[17] Elezovic NR, Babic BM, Radmilovic VR, Vracar LM, Krstajic N V. Synthesis and characterization of MoO_x-Pt/C and TiO_x-Pt/C nano-catalysts for oxygen reduction. Electrochim Acta 2009;54:2404–9. https://doi.org/10.1016/j.electacta.2008.03.015.

[18] Qian C, Guo X, Zhang W, Yang H, Qian Y, Xu F, et al. Co_3O_4 nanoparticles on porous bio-carbon substrate as catalyst for oxygen reduction reaction. Microporous Mesoporous Mater 2019;277:45–51. https://doi.org/10.1016/J.MICROMESO.2018.10.020.

[19] Shanmugapriya S, Nithya VD, Rajalakshmi A, Sivaranjani K, Bharathi P, Shalini S, et al. Sonochemical synthesis, structural, electrical transport and magnetic properties of $NiWO_4$ nanoparticles. J Mater Sci Mater Electron 2020;31:15616–26.

[20] Scheffer B, Molhoek P, Moulijn JA. Temperature-programmed reduction of $NiOWO_3/Al_2O_3$ Hydrodesulphurization catalysts. Appl Catal 1989;46:11–30. https://doi.org/10.1016/S0166-9834(00)81391-3.

[21] Bi Y, Nie H, Li D, Zeng S, Yang Q, Li M. $NiWO_4$ nanoparticles: a promising catalyst for hydrodesulfurization. Chem Commun 2010;46:7430–2. https://doi.org/10.1039/C0CC01977A.

[22] Stern DL, Grasselli RK. Propane Oxydehydrogenation over Metal Tungstates. J Catal 1997;167:570–2. https://doi.org/10.1006/jcat.1997.1570.

[23] Guo F, Guo S, Qiu Z, Zhao L, Xiang H. Effects of impregnation methods and drying conditions on quinoline hydrodenitrogenation over Ni-W based catalysts. J Braz Chem Soc 2014;25:750–8.

[24] Xu J, Holthaus P, Yang N, Jiang S, Heupel A, Schönherr H, et al. Catalytic tar removal using $TiO_2/NiWO_4$-Ni_5TiO_7 films. Appl Catal B Environ 2019;249:155–62. https://doi.org/10.1016/j.apcatb.2019.03.006.

[25] Quintana-Melgoza JM, Gómez-cortés A, Avalos-Borja M. REDUCTION OF NO BY CO OVER $NiWO_4$, NiO, AND WO_3 CATALYSTS. React Kinet Catal Lett 2002;76:131–40. https://doi.org/10.1023/A:1015629815029.

[26] Pourmortazavi SM, Rahimi-Nasrabadi M, Khalilian-Shalamzari M, Zahedi MM, Hajimirsadeghi SS, Omrani I. Synthesis, structure characterization and catalytic activity of nickel tungstate nanoparticles. Appl Surf Sci 2012;263:745–52. https://doi.org/10.1016/j.apsusc.2012.09.153.

[27] Yin X-L, Li L-L, Gao G-M, Lu Y, Shang Q-Q, Zhao H-T, et al. Direct Z-Scheme $NiWO_4$/CdS nanosheets-on-nanorods nanoheterostructure for efficient visible-light-driven H_2 generation. Int J

Hydrogen Energy 2022;47:9895–904. https://doi.org/10.1016/j.ijhydene.2022.01.068.

[28] Montini T, Gombac V, Hameed A, Felisari L, Adami G, Fornasiero P. Synthesis, characterization and photocatalytic performance of transition metal tungstates. Chem Phys Lett 2010;498:113–9. https://doi.org/10.1016/j.cplett.2010.08.026.

[29] Hitha H, Jose A, John M, Varghese T. Structural and optical modification of $NiWO_4$ – Formation of $NiWO_4$/SnPc nanocomposite for improved photocatalytic activity. Mater Chem Phys 2020;239:122080. https://doi.org/10.1016/j.matchemphys.2019.122080.

[30] Karthiga R, Kavitha B, Rajarajan M, Suganthi A. Photocatalytic and antimicrobial activity of $NiWO_4$ nanoparticles stabilized by the plant extract. Mater Sci Semicond Process 2015;40:123–9. https://doi.org/10.1016/j.mssp.2015.05.037.

[31] Rosal FJO, Gouveia AF, Sczancoski JC, Lemos PS, Longo E, Zhang B, et al. Electronic structure, growth mechanism, and sonophotocatalytic properties of sphere-like self-assembled $NiWO_4$ nanocrystals. Inorg Chem Commun 2018;98:34–40. https://doi.org/10.1016/j.inoche.2018.10.001.

[32] Wang Y, Shen C, Niu L, Sun Z, Ruan F, Xu M, et al. High rate capability of mesoporous $NiWO_4$–$CoWO_4$ nanocomposite as a positive material for hybrid supercapacitor. Mater Chem Phys 2016;182:394–401. https://doi.org/10.1016/j.matchemphys.2016.07.047.

[33] Kumar RD, Andou Y, Karuppuchamy S. Synthesis and characterization of nanostructured Ni-WO_3 and $NiWO_4$ for supercapacitor applications. J Alloys Compd 2016;654:349–56. https://doi.org/10.1016/j.jallcom.2015.09.106.

[34] Tian J, Xue Y, Yu X, Pei Y, Zhang H, Wang J. Solvothermal synthesis of $NiWO_4$ nanostructure and its application as a cathode material for asymmetric supercapacitors. RSC Adv 2018;8:41740–8. https://doi.org/10.1039/C8RA09128E.

[35] Hai G, Huang J, Cao L, Kajiyoshi K, Wang L, Feng L. Hierarchical $W_{18}O_{49}$/$NiWO_4$/NF heterojunction with tuned composition and charge transfer for efficient water splitting. Appl Surf Sci 2021;562:150145. https://doi.org/10.1016/J.APSUSC.2021.150145.

[36] Srirapu VKVP, Kumar A, Srivastava P, Singh RN, Sinha ASK. Nanosized $CoWO_4$ and $NiWO_4$ as efficient oxygen-evolving electrocatalysts. Electrochim Acta 2016;209:75–84. https://doi.org/10.1016/j.electacta.2016.05.042.

[37] Du X, Shao Q, Zhang X. Metal tungstate dominated $NiCo_2O_4$@$NiWO_4$ nanorods arrays as an efficient electrocatalyst for water splitting. Int J Hydrogen Energy 2019;44:2883–8. https://doi.org/https://doi.org/10.1016/j.ijhydene.2018.12.061.

[38] Wang J, Jang H, Li G, Kim MG, Wu Z, Liu X, et al. Efficient electrocatalytic conversion of N_2 to NH_3 on $NiWO_4$ under ambient conditions. Nanoscale 2020;12:1478–83. https://doi.org/10.1039/C9NR08777J.

[39] Adzic, R.R., Marinkovic NS. Elecrocatalysts for alcohol oxidation in fuel cells. 6,183,894 B1, 2001.

[40] Shi M, Tong X, Li W, Fang J, Chen L, Ma C. Enhanced Electrocatalytic Oxygen Reduction on $NiWO_x$ Solid Solution with Induced Oxygen Defects. ACS Appl Mater \& Interfaces 2017;9:34990–5000. https://doi.org/10.1021/acsami.7b10891.

[41] A. Halder, M. Zhang QC. Advanced Catalytic Materials - Photocatalysis and Other Current Trends.

2015. https://doi.org/10.5772/61808.

[42] Tan H, Kim J, Lin J, Li C, Alsheri SM, Ahamad T, et al. A facile surfactant-assisted synthesis of carbon-supported dendritic Pt nanoparticles with high electrocatalytic performance for the oxygen reduction reaction. Microporous Mesoporous Mater 2019;280:1–6. https://doi.org/10.1016/J.MICROMESO.2019.01.020.

[43] Geetanjali, Rani R, Kumar S. Microbial community dynamics of microbial fuel cell in response to $NiWO_4$/rGO nanocomposites as electrocatalyst and its correlation with electrochemical properties. J Environ Chem Eng 2021;9:104668. https://doi.org/10.1016/J.JECE.2020.104668.

[44] Ahmed J, Ahamad T, Ubaidullah M, Al-Enizi AM, Alhabarah AN, Alhokbany N, et al. rGO supported $NiWO_4$ nanocomposites for hydrogen evolution reactions. Mater Lett 2019;240:51–4. https://doi.org/10.1016/j.matlet.2018.12.114.

[45] Li F, Long L, Weng Y. A Review on the Contemporary Development of Composite Materials Comprising Graphene/Graphene Derivatives. Adv Mater Sci Eng 2020;2020:7915641. https://doi.org/10.1155/2020/7915641.

[46] Cataldi P, Athanassiou A, Bayer IS. Graphene Nanoplatelets-Based Advanced Materials and Recent Progress in Sustainable Applications. Appl Sci 2018;8. https://doi.org/10.3390/app8091438.

[47] Chung DDL. A review of exfoliated graphite. J Mater Sci 2016;51:554–68. https://doi.org/10.1007/s10853-015-9284-6.

[48] Zhang Q, Wang YC, Bailey CG, Yuen RKK, Parkin J, Yang W, et al. Quantifying effects of graphene nanoplatelets on slowing down combustion of epoxy composites. Compos Part B Eng 2018;146:76–87. https://doi.org/10.1016/j.compositesb.2018.03.049.

[49] Argüello JA, Cerpa A, Moreno R. Reinforcing effect of graphene nanoplatelets in the electrochemical behaviour of manganese oxide-based supercapacitors produced by EPD. Ceram Int 2019;45:14316–21. https://doi.org/10.1016/j.ceramint.2019.04.145.

[50] Masouras A, Giannopoulos D, Hasa B, Katsaounis A, Kostopoulos V. Hybrid graphene nanoplatelet/manganese oxide electrodes for solid-state supercapacitors and application to carbon fiber composite multifunctional materials. J Energy Storage 2019;23:515–25. https://doi.org/10.1016/j.est.2019.04.025.

[51] Lim DG, Zhao Y, Manikandan P, Adams RA, Youngblood JP, Pol VG. Tailored sonochemical synthesis of V_2O_5|graphene nanoplatelets composites and its enhanced Li-ion insertion properties. Mater Res Bull 2019;114:37–44. https://doi.org/10.1016/j.materresbull.2019.02.014.

[52] Devrim Y, Arıca ED, Albostan A. Graphene based catalyst supports for high temperature PEM fuel cell application. Int J Hydrogen Energy 2018;43:11820–9. https://doi.org/10.1016/j.ijhydene.2018.03.047.

[53] Daş E, Alkan Gürsel S, Işıkel Şanlı L, Bayrakçeken Yurtcan A. Thermodynamically controlled Pt deposition over graphene nanoplatelets: Effect of Pt loading on PEM fuel cell performance. Int J Hydrogen Energy 2017;42:19246–56. https://doi.org/10.1016/j.ijhydene.2017.06.108.

[54] Ahmed MI, Adam A, Khan A, Siddiqui MN, Yamani ZH, Qamar M. Synthesis of mesoporous $NiWO_4$ nanocrystals for enhanced photoelectrochemical water oxidation. Mater Lett 2016;177:135–8. https://doi.org/10.1016/J.MATLET.2016.04.143.

[55] Mallick S, Mondal A, Raj CR. Rationally designed mesoporous carbon-supported Ni–$NiWO_4$@NiS nanostructure for the fabrication of hybrid supercapacitor of long-term cycling stability. J Power Sources 2020;477:229038. https://doi.org/10.1016/J.JPOWSOUR.2020.229038.

[56] Peng T, Liu C, Hou X, Zhang Z, Wang C, Yan H, et al. Control Growth of Mesoporous Nickel Tungstate Nanofiber and Its Application as Anode Material for Lithium-Ion Batteries. Electrochim Acta 2017;224:460–7. https://doi.org/10.1016/J.ELECTACTA.2016.11.154.

[57] Vass Á, Borbáth I, Bakos I, Pászti Z, Sajó IE, Tompos A. Novel Pt Electrocatalysts: Multifunctional Composite Supports for Enhanced Corrosion Resistance and Improved CO Tolerance. Top Catal 2018;61:1300–12. https://doi.org/10.1007/s11244-018-0988-0.

[58] Vinoth Kumar, J., Arunpadian, M., Sivaganesh, D., Nagarajan ER. 3D Sphere-like Nickel Tungstate Catalyst for Destroying of Organophosphate Pesticide Methyl Parathion. Int J Eng Adv Technol 2019;9:216–9.

[59] Quintana-Melgoza JM, Cruz-Reyes J, Avalos-Borja M. Synthesis and characterization of $NiWO_4$ crystals. Mater Lett 2001;47:314–8. https://doi.org/10.1016/S0167-577X(00)00272-X.

[60] Ross-Medgaarden EI, Wachs IE. Structural Determination of Bulk and Surface Tungsten Oxides with UV−vis Diffuse Reflectance Spectroscopy and Raman Spectroscopy. J Phys Chem C 2007;111:15089–99. https://doi.org/10.1021/jp074219c.

[61] Harshan H, Priyanka KP, Sreedevi A, Jose A, Varghese T. Structural, optical and magnetic properties of nanophase $NiWO_4$ for potential applications. Eur Phys J B 2018;91:287. https://doi.org/10.1140/epjb/e2018-90382-3.

[62] Lima NA, Alencar LDS, Siu-Li M, Feitosa CAC, Mesquita A, M'peko J-C, et al. $NiWO_4$ powders prepared via polymeric precursor method for application as ceramic luminescent pigments. J Adv Ceram 2020;9:55–63. https://doi.org/10.1007/s40145-019-0347-z.

[63] Kuzmin A, Kalinko A, Evarestov RA. Ab initio LCAO study of the atomic, electronic and magnetic structures and the lattice dynamics of triclinic $CuWO_4$. Acta Mater 2013;61:371–8. https://doi.org/10.1016/j.actamat.2012.10.002.

[64] Kudin KN, Ozbas B, Schniepp HC, Prud'homme RK, Aksay IA, Car R. Raman Spectra of Graphite Oxide and Functionalized Graphene Sheets. Nano Lett 2008;8:36–41. https://doi.org/10.1021/nl071822y.

[65] Tian Z, Liu C, Li Q, Hou J, Li Y, Ai S. Nitrogen- and oxygen-functionalized carbon nanotubes supported Pt-based catalyst for the selective hydrogenation of cinnamaldehyde. Appl Catal A Gen 2015;506:134–42. https://doi.org/10.1016/j.apcata.2015.08.023.

[66] Tuinstra F, Koenig JL. Raman Spectrum of Graphite. J Chem Phys 1970;53:1126–30. https://doi.org/10.1063/1.1674108.

[67] Nieto A, Kumar A, Lahiri D, Zhang C, Seal S, Agarwal A. Oxidation behavior of graphene nanoplatelet reinforced tantalum carbide composites in high temperature plasma flow. Carbon N Y 2014;67:398–408. https://doi.org/10.1016/j.carbon.2013.10.010.

[68] Zhang Q, Wang YC, Soutis C, Bailey CG, Hu Y. Fire Safety Assessment of Epoxy Composites Reinforced by Carbon Fibre and Graphene. Appl Compos Mater 2020;27:619–39.

https://doi.org/10.1007/s10443-020-09824-4.

[69] Sing KSW. Reporting physisorption data for gas/solid systems with special reference to the determination of surface area and porosity (Recommendations 1984). Pure Appl Chem 1985;57:603–19. doi:10.1351/pac198557040603.

[70] Mahmud RA, Shafawi AN, Ahmed Ali K, Putri LK, Md Rosli NI, Mohamed AR. Graphene nanoplatelets with low defect density as a synergetic adsorbent and electron sink for ZnO in the photocatalytic degradation of Methylene Blue under UV–vis irradiation. Mater Res Bull 2020;128:110876. https://doi.org/10.1016/j.materresbull.2020.110876.

[71] Kim KS, Winograd N. X-ray photoelectron spectroscopic studies of nickel-oxygen surfaces using oxygen and argon ion-bombardment. Surf Sci 1974;43:625–43. https://doi.org/10.1016/0039-6028(74)90281-7.

[72] Christ B. PDF Handbook of Monochromatic XPS of Commercially Pure Binary Oxides. XPS International LLC, Mountain View, CA; 2018.

[73] Naumkin AK-V, Gaarenstroom SW, Cedric JP. NIST X-ray Photoelectron Spectroscopy Database NIST Standard Reference Database 20, Version 4.1. NIST X-Ray Photoelectron Spectrosc Database NIST Stand Ref Database 20, Version 41 2000. https://doi.org/10.18434/T4T88K.

[74] Preda L, Spataru N, Calderon Moreno JM, Somacescu S, Marcu M. Graphene Incorporation as a Propitious Approach for Improving the Oxygen Reduction Reaction (ORR) Activity of Self-assembled Polycrystalline $NiCo_2O_4$–NiO. Electrocatalysis 2020;11:443–53. https://doi.org/10.1007/s12678-020-00605-y.

[75] Zhou R, Zheng Y, Jaroniec M, Qiao S-Z. Determination of the Electron Transfer Number for the Oxygen Reduction Reaction: From Theory to Experiment. ACS Catal 2016;6:4720–8. https://doi.org/10.1021/acscatal.6b01581.

[76] Nagy B, Bakos I, Bertóti I, Domán A, Menyhárd A, Mohai M, et al. Synergism of nitrogen and reduced graphene in the electrocatalytic behavior of resorcinol - Formaldehyde based carbon aerogels. Carbon N Y 2018;139:872–9. https://doi.org/10.1016/j.carbon.2018.07.061.

[77] Islam MT, Hasan MM, Shabik MF, Islam F, Nagao Y, Hasnat MA. Electroless deposition of gold nanoparticles on a glassy carbon surface to attain methylene blue degradation via oxygen reduction reactions. Electrochim Acta 2020;360:136966. https://doi.org/10.1016/j.electacta.2020.136966.

[78] Masa J, Batchelor-McAuley C, Schuhmann W, Compton RG. Koutecky-Levich analysis applied to nanoparticle modified rotating disk electrodes: Electrocatalysis or misinterpretation. Nano Res 2014;7:71–8. https://doi.org/10.1007/s12274-013-0372-0.

[79] Batchelor-McAuley C, Compton RG. Thin-Film Modified Rotating Disk Electrodes: Models of Electron-Transfer Kinetics for Passive and Electroactive Films. J Phys Chem C 2014;118:30034–8. https://doi.org/10.1021/jp5104593.

[80] Wang JX, Markovic NM, Adzic RR. Kinetic Analysis of Oxygen Reduction on Pt(111) in Acid Solutions: Intrinsic Kinetic Parameters and Anion Adsorption Effects. J Phys Chem B 2004;108:4127–33. https://doi.org/10.1021/jp037593v.

[81] A.J. Bard and L.R. Faulkner. Electrochemical Methods: Fundamentals and Applications. Wiley; 2000.

[82] Blizanac BB, Ross PN, Marković NM. Oxygen Reduction on Silver Low-Index Single-Crystal Surfaces in Alkaline Solution: Rotating Ring DiskAg(hkl) Studies. J Phys Chem B 2006;110:4735–41. https://doi.org/10.1021/jp056050d.

[83] Holewinski A, Linic S. Elementary Mechanisms in Electrocatalysis: Revisiting the ORR Tafel Slope. J Electrochem Soc 2012;159:H864–70. https://doi.org/10.1149/2.022211jes.

[84] Chen W, Xiang Q, Peng T, Song C, Shang W, Deng T, et al. Reconsidering the Benchmarking Evaluation of Catalytic Activity in Oxygen Reduction Reaction. IScience 2020;23:101532. https://doi.org/10.1016/j.isci.2020.101532.

[85] Agbo P, Danilovic N. An Algorithm for the Extraction of Tafel Slopes. J Phys Chem C 2019;123:30252–64. https://doi.org/10.1021/acs.jpcc.9b06820.

[86] Stassi A, D'urso C, Baglio V, Di Blasi A, Antonucci V, Arico AS, et al. Electrocatalytic behaviour for oxygen reduction reaction of small nanostructured crystalline bimetallic Pt–M supported catalysts. J Appl Electrochem 2006;36:1143–9. https://doi.org/10.1007/s10800-006-9197-9.

[87] Meng H, Shen PK. Tungsten Carbide Nanocrystal Promoted Pt/C Electrocatalysts for Oxygen Reduction. J Phys Chem B 2005;109:22705–9. https://doi.org/10.1021/jp054523a.

[88] Schmidt TJ, Gasteiger HA, Behm RJ. Rotating Disk Electrode Measurements on the CO Tolerance of a High- Surface Area Pt/Vulcan Carbon Fuel Cell Catalyst. J Electrochem Soc 1999;146:1296–304. https://doi.org/10.1149/1.1391761.

[89] Schmidt TJ, Gasteiger HA, Stäb GD, Urban PM, Kolb DM, Behm RJ. Characterization of High-Surface-Area Electrocatalysts Using a Rotating Disk Electrode Configuration. J Electrochem Soc 1998;145:2354–8. https://doi.org/10.1149/1.1838642.

[90] Maiorova NA, Mikhailova AA, Khazova OA, Grinberg VA. Thin-film rotating disk electrode as a tool for comparing the activity of catalysts in the hydrogen oxidation reaction. Russ J Electrochem 2006;42:331–8. https://doi.org/10.1134/S1023193506040082.

[91] Schmidt TJ, Jusys Z, Gasteiger HA, Behm RJ, Endruschat U, Boennemann H. On the CO tolerance of novel colloidal PdAu/carbon electrocatalysts. J Electroanal Chem 2001;501:132–40. https://doi.org/10.1016/S0022-0728(00)00516-7.

[92] Nagy G, Schiller R. Hydrogen in tungsten bronzes: mechanism of hydrogen intercalation. Int J Hydrogen Energy 1989;14:567–72. https://doi.org/10.1016/0360-3199(89)90115-8.

[93] Tseung ACC, Shen PK, Chen KY. Precious metal/hydrogen bronze anode catalysts for the oxidation of small organic molecules and impure hydrogen. J Power Sources 1996;61:223–5. https://doi.org/10.1016/S0378-7753(96)02352-X.

[94] Zeng J, Yang Lee J. Ruthenium-free, carbon-supported cobalt and tungsten containing binary & ternary Pt catalysts for the anodes of direct methanol fuel cells. Int J Hydrogen Energy 2007;32:4389–96. https://doi.org/10.1016/j.ijhydene.2007.03.012.

[95] Mohamed MM, Khairy M, Eid S. Polyethylene glycol assisted one-pot hydrothermal synthesis of $NiWO_4/WO_3$ heterojunction for direct Methanol fuel cells. Electrochim Acta 2018;263:286–98. https://doi.org/10.1016/j.electacta.2018.01.063.

[96] Liu L, Corma A. Metal Catalysts for Heterogeneous Catalysis: From Single Atoms to Nanoclusters and

Nanoparticles. Chem Rev 2018;118:4981–5079. https://doi.org/10.1021/acs.chemrev.7b00776.

[97] Siburian R, Ali AMM, Sebayang K, Supeno M, Tarigan K, Simanjuntak C, et al. The loading effect of Pt clusters on Pt/graphene nano sheets catalysts. Sci Rep 2021;11:2532. https://doi.org/10.1038/s41598-020-80472-1.